

# Distribution and Kinematics of the Circum-nuclear Molecular Gas in the Seyfert 1 Galaxy NGC 3227

E. Schinnerer<sup>1</sup>, A. Eckart, L.J. Tacconi

Max-Planck-Institut für extraterrestrische Physik, 85740 Garching, Germany

Received \_\_\_\_\_; accepted \_\_\_\_\_

---

<sup>1</sup>Present address: California Institute of Technology, Pasadena, CA 91125

<sup>2</sup>Ap. J. accepted

## ABSTRACT

We present new interferometric observations of the  $^{12}\text{CO}$  (1-0) ,  $^{12}\text{CO}$  (2-1) , and HCN (1-0) molecular line emission in NGC 3227 obtained with the IRAM Plateau de Bure interferometer (PdBI). We achieved an unprecedented angular resolution in the  $^{12}\text{CO}$  (2-1) line of about  $0.6''$  corresponding to only about 80 pc at a distance of 17.3 Mpc. The mapped  $^{12}\text{CO}$  emission is concentrated in the inner  $8''$  and accounts for 20% of the total 30 m  $^{12}\text{CO}$  line flux. The  $^{12}\text{CO}$  emission is resolved into an asymmetric nuclear ring with a diameter of about  $3''$ . The HCN line emission is mostly unresolved at our resolution of  $\sim 2.4''$  and contains all of the single dish flux. We have decomposed the observed molecular gas motions into a circular and non-circular component revealing that about 80 % of the gas in the circum-nuclear region exhibits pure circular rotation. We find evidence for bar streaming onto the nuclear ring and a redshifted emission knot on the ring perimeter.

In the central arcsecond the gas shows apparent counter rotation. This behavior can be best explained by a warping of the inner molecular gas disk rather than gas motion in a nuclear bar potential. We detected molecular gas at a distance from the nucleus of only  $\sim 13$  pc with a velocity of about 75 km/s with respect to the systemic velocity and find that within the central arcsecond the rotation curve is rising again. This is the first time that millimetric CO-line emission has been detected interferometrically at such small distances to the nucleus of a Seyfert galaxy. These measurements indicate a lower limit on the enclosed mass of about  $2 \times 10^7 M_{\odot}$  in the inner 25 pc.

*Subject headings:* galaxies: ISM - galaxies: nuclei of - radio lines: ISM - galaxies: individual (NGC 3227)

## 1. INTRODUCTION

The distribution of circum-nuclear molecular gas plays an important role in the proposed unified scheme for Seyfert galaxies. In the standard picture a torus of dense molecular gas and dust is surrounding the black hole and its accretion disk (e.g. overviews by Antonucci 1993 and Peterson 1997, see also Pier & Krolik 1992, 1993, Edelson & Malkan 1987). As the relative orientation of the AGN to the plane of its host galaxy is probably random the appearance of the AGN as Seyfert 1 or Seyfert 2 nucleus depends only on whether the viewing angle onto the central engine is blocked by the torus or not. There are two important questions arising for the distribution and kinematics of the circum-nuclear molecular gas:

(1) Is the circum-nuclear molecular gas already participating in the obscuration of the AGN? Recent observations of about 250 nearby active galaxies with the HST from Malkan, Gorjian & Tam (1998) suggest that molecular material at distances of about 100 pc is responsible for the obscuration of the nucleus rather than a nuclear torus. Similarly Cameron et al. (1993) and Schinnerer, Eckart & Tacconi (1999) find indications for a more complex picture in NGC 1068.

(2) What is the fueling mechanism for AGNs? As a very effective mechanism nuclear bars are considered to bring the molecular gas to small radii and fuel the central engine (e.g. Shlosman, Frank & Begelman 1989). However, Regan & Mulchaey (1999) searched in 12 nearby Seyfert galaxies with little success for signatures of strong nuclear bars by combining HST NICMOS 1.6  $\mu\text{m}$  images with HST optical images to study the dust morphology (see also Martini & Pogge 1999).

The recent improvements in mm-interferometry now allow one to obtain sub-arcsecond resolution observations of the molecular line emission in combination with high spectral resolution and high sensitivity. This combination is ideal to study the kinematics and distribution of molecular gas in the circum-nuclear region of nearby Seyfert galaxies.

NGC3227 (Arp 94b) is a Seyfert 1 galaxy located at a distance of 17.3 Mpc (group distance; Garcia 1993; see also Tab. 1). Rubin & Ford (1968) studied the system NGC 3226/7 for the first time in the optical. In NGC 3227 they found indications for a nuclear outflow as well as a spiral arm that stretches toward the close elliptical companion. The NLR is extended towards the northeast (Mundell et al. 1992a, Schmitt & Kinney 1996) and the BLR clearly shows variations in the optical continuum and line emission (Salamanca et al. 1994, Winge et al. 1995).

NGC 3227 is classified as a SAB(s) pec in the RC3 catalog (de Vaucouleurs et al. 1991). Due to its inclination the end of the bar and the starting points of the spiral arms are difficult to identify. As indicated by optical and NIR observations (Mulchaey, Regan, Kundu 1997, De Robertis et al. 1998) the galaxy has probably a bar with 6.7 kpc - 8.4 kpc radius and a position angle of about  $-20^\circ$  relative to the major kinematic axis. Mundell et al. (1995b) studied the system NGC 3226/7 in the HI line emission. Two gas plumes north and south of the system are seen with velocities between about 1200 km/s and 1300 km/s.

The HI gas of the plumes with the largest spatial separation from NGC 3227 also shows the largest velocity difference to NGC 3227 ( $v_{sys} = 1110 \pm 10$  km/s; derived in section 4). These clumps can be identified with tidal tails which are often observed in interacting galaxies.

Here we mainly study the distribution and kinematics of the molecular gas in the central few arcseconds of NGC 3227. The observations are summarized in section 2 followed by the description of the interferometric data (section 3). In section 4 we outline molecular gas kinematics including the derivation of the rotation curve and a discussion of the general structural and dynamical properties. A decomposition of the molecular gas in NGC 3227 into components of circular and non-circular motion is given in section 5 (and Appendix A). The mass and thickness of the molecular gas disk are derived in section 6. In section 7 (and Appendix B and C) a 3-dimensional analysis of the kinematics in the inner 1'' (85 pc) in NGC 3227 in the framework of a bar and warp model for the gas motion is presented. The final summary and implications are given in section 8.

## 2. OBSERVATIONS AND DATA REDUCTION

The  $^{12}\text{CO}$  (1-0) and  $^{12}\text{CO}$  (2-1) lines were observed in January/February 1997 using the IRAM PdB interferometer with 5 antennas in its A, B1 and B2 configuration providing 30 baselines from 40 m to 408 m. The resulting resolution is  $1.5'' \times 0.9''$  (PA  $34^\circ$ ) at 2.6 mm and  $0.7'' \times 0.5''$  (PA  $31^\circ$ ) at 1.3 mm using uniform weighting. We applied standard data reduction and calibration (15% accuracy at 2.6 and 1.3 mm) procedures. After cleaning we reconvolved data with a CLEAN beam of FWHM  $1.2''$  for  $^{12}\text{CO}$  (1-0) and FWHM  $0.6''$  for the  $^{12}\text{CO}$  (2-1). To increase the S/N we smoothed the data spectrally to a resolution of 20 km/s in both lines. In addition a  $^{12}\text{CO}$  (2-1) data set with a spectral resolution of 7 km/s was made ranging from -182 km/s to 182 km/s since only this interval was covered by all three configurations.

The HCN (1-0) line was observed between March 1995 and March 1996 using the IRAM PdB interferometer with 4 antennas in its B1, B2, C1 and C2 configuration providing baselines from 24 m to 288 m. The spatial resolution is  $3.3'' \times 1.7''$  (PA  $42^\circ$ ) using natural weighting. The uncertainties of the flux calibration are about 15 %. For the interferometric observations we used a velocity of  $v_{obs} = 1154$  km/s which is 44 km/s larger than the systemic velocity of  $v_{sys} = 1110$  km/s derived from the data (section 4).

## 3. RESULTS

The IRAM 30 m data (Schinnerer et al. in prep.) show an elongation of the nuclear line emission at a PA of  $\sim 130^\circ$ . A comparison to published data reveals that even the 30 m telescope already starts to spatially resolve parts of the central 2 kpc diameter emission. At high angular resolution most of the molecular gas is located in a  $3''$  diameter circum-nuclear ring. In the following subsections we describe the distribution and kinematics of the

molecular gas as observed with the PdBI in the  $^{12}\text{CO}(1-0)$ ,  $^{12}\text{CO}(2-1)$ , and the  $\text{HCN}(1-0)$  line. The detection of molecular line emission at radii as small as 13 pc is used to estimate an upper limit to the enclosed nuclear mass. No millimeter radio continuum emission was detected by our interferometric observations. The corresponding upper limits are 8 mJy at 1.3 mm and 5 mJy at 2.6 mm.

### 3.1. The extended emission

The  $^{12}\text{CO}$  emission mapped with the PdBI is concentrated in an uneven ring-like structure in the inner 6'' (500 pc; Fig. 1). The eastern part is about six times brighter than the western part (Fig. 1). In the following we refer to this structure as the *ring*. In the channel maps  $^{12}\text{CO}$  (1-0) line emission is seen from -260 km/s to 220 km/s (relative to the central velocity  $v_{\text{obs}} = 1154$  km/s we used for the observations) and from -240 km/s to 180 km/s for the  $^{12}\text{CO}$  (2-1) line at a spectral resolution of 20 km/s. The difference in velocity range is probably due to the fact that the smaller 0.6'' beam of the  $^{12}\text{CO}$  (2-1) line has already resolved some emission which is still detected in the  $^{12}\text{CO}$  (1-0) beam of 1.2''.

A comparison to single dish measurements shows that the PdBI  $^{12}\text{CO}$  (1-0) and  $^{12}\text{CO}$  (2-1) maps contain about 20 % and 10 % of the total line flux, respectively. Combined with the results from the 30 m maps (Schinnerer et al. in prep.) this means that most of the remaining  $^{12}\text{CO}$  gas is distributed in a fairly smooth gas disk, and the structures seen in the PdBI maps are the main concentrations of the molecular gas. However, the  $^{12}\text{CO}$  line flux observed by the PdBI traces the compact circum-nuclear gas component that constitutes the reservoir out of which both the nucleus as well as circum-nuclear star formation can be fed.

A much weaker additional component (*molecular bar*) is detected east and west of the center. This component stretches out to a radius of about 7'' (590 pc). The east and west parts of the bar have a NS-offset of about 3'' connecting the NW-region with the circum-nuclear ring (Fig. 1). In the de-projected map this component resembles a bar which encloses an angle of about  $85^\circ$  with the kinematic major axis (Fig. 2). For de-projection the intensity maps were rotated by the position angle so that the kinematic major axis is parallel to the  $x$ -axis. The  $y$ -axis was then corrected via  $y = y'/\cos(i)$ , where  $i$  is the inclination.

In addition emission regions to the north-west, south-east and south (*NW-region*, *SW-region*, *S-region*; Fig. 2) lie in a de-projected spatial distance of 10'' to 20'' from the center and have typical sizes of about 1.5'' to 2''. The NW- and SE-region are stronger in the  $^{12}\text{CO}$  (1-0) line than in the  $^{12}\text{CO}$  (2-1) line whereas the S-region is more prominent in the  $^{12}\text{CO}$  (2-1) line. This might indicate that the molecular line emission in the S-region is partly due to optically thin gas. The NW-region lies at the tip of the molecular bar and is also twice as bright as the SE-region in the  $^{12}\text{CO}$  (1-0) line emission.

### 3.2. The nuclear emission

Over a velocity range from -140 km/s to 35 km/s we detect emission with an extent  $\sim 0.6''$  at the dynamical center. In all pv-diagrams the structure of this component appears to be S-shaped and symmetric both with respect to the central position and with respect to a velocity about 19 km/s below the systemic velocity  $v_{sys;HI} = 1135$  km/s derived from HI observations by Mundell et al. 1995b (44 km/s below the central velocity of  $v_{obs} = 1154$  km/s we assumed for the observations).

*The position of the dynamical center:* To derive the exact position of the dynamical center we fitted a Gaussian to the nuclear component in the channel map at -63 km/s. We chose that map since its velocity is relatively close to the true systemic velocity and the nuclear component is clearly separated from the emission in the ring. The nucleus is positioned  $(0.28 \pm 0.02)''$  west and  $(0.84 \pm 0.03)''$  north of the interferometer phase center of RA  $10^h 23^m 30.590^s$  and DEC  $19^\circ 51' 54.00''$  (J2000.0). We note that the position of the phase center may itself have an error of up to  $0.2''$ . With this uncertainty the positions of the northern and southern radio component (Mundell et al. 1995b) are both included in our error budget.

### 3.3. The HCN (1-0) Data

The HCN (1-0) line emission in NGC 3227 was observed with the IRAM 30 m (Schinnerer et al. in prep.) as well as the PdBI (Fig. 3). The comparison of both measurements shows that the PdBI map contains the total flux of the 30 m observation. The HCN (1-0) line emission is concentrated in a barely resolved nuclear source. A Gaussian fit provides a source size of  $(2.67 \pm 0.24)''$  very similar to the FWHM of the beam of  $2.4''$ . Therefore the HCN source structure is much more compact than the  $^{12}\text{CO}$  ring structure. The strongest HCN(1-0) emission (about twice as strong as in the neighboring channel maps) is found at -40 km/s (close to the systemic velocity) indicating a strong nuclear component. The position of the peak within its errors in this map is identical to the position of the dynamical center. The shape of the pv-diagram (Fig. 5) along the kinematic major axis is different from that of the strong and extended  $^{12}\text{CO}$  (1-0) line emission (Fig. 5). The shape of the HCN(1-0) pv-diagram is similar to the inner part of the  $^{12}\text{CO}$  (2-1) pv-diagram at 7 km/s (Fig. 6) convolved to a lower resolution. This indicates that most of the HCN(1-0) emission is coming from a region with  $\leq 0.6''$  diameter.

## 4. MOLECULAR GAS KINEMATICS

In this section we describe the properties of the molecular gas kinematics in the circum-nuclear region of NGC 3227. We outline how we derived a rotation curve and what the expected dynamical resonances in conjunction with the possible kpc-scale bar in

NGC 3227 are.

#### 4.1. General kinematic properties of NGC 3227

Mundell et al. (1995b) detected in their HI study of the system NGC 3226/7 an HI cloud or dwarf galaxy about  $60''$  (5 kpc) west of the nucleus of NGC 3227. The observed features (tidal tails, enhanced star formation at the position of the western spiral arm) indicate that the interaction with NGC 3226 and probably also the HI cloud is ongoing. On the other hand the HI disk is relatively undisturbed, since its velocity field is in good agreement with an inclined rotating disk (Mundell et al. 1995b). González Delgado & Perez (1998) observed HII regions in NGC 3227 in their  $H\alpha$  emission. The HII regions show an offset to the NW and SE relative to the major axis of the galaxy in agreement with the position of a bar. Theoretical calculations (e.g. Athanassoula 1992a) predict that gas at the leading side of the bar is shocked and compressed, favoring the formation of stars there. This indicates that NGC 3227 is rotating clockwise. Therefore the spiral arms are trailing and the southwestern side is closer to the observer. The location of prominent dust lanes seen in the optical HST images of Malkan et al. (1998) are consistent with this geometry.

#### 4.2. The nuclear molecular gas

*The peculiar nuclear kinematics:* In the  $^{12}\text{CO}$  (2-1) data set with a spectral resolution of 7 km/s the contrast of the more compact structures was enhanced over that of the more extended components to allow for a detailed study of the inner  $1''$ . The pv-diagrams presented in Fig. 6 have now a nominal resolution of  $0.3''$ . Along all position angles the emission in the inner  $1''$  does not drop linearly to zero at the center. Along the kinematic major axis an apparent counter rotation is observed between  $0.2'' \leq r \leq 0.5''$  (see Fig. 5). For even smaller radii the velocity flips back again to the rotation sense of the outer structure at  $r > 0.5''$ . This behavior forms a S-shape in the inner  $1''$  of the pv-diagrams. These changes in the rotation sense are present in all pv-diagrams.

*The enclosed nuclear mass:* If the velocity of the nuclear emission inside  $r \leq 0.2''$  is due to Keplerian motion of molecular gas these data can be used to estimate the enclosed mass. Assuming an inclined disk the position angle under which these two emission regions have the largest angular separation of  $0.28''$  at a position angle of  $PA \sim 110^\circ$ . This is not coincident with the position angles of other components like the radio jet ( $\sim -10^\circ$ ; Mundell et al. 1995b), the [O III] ionization cone ( $\sim 15^\circ$ ; Schmitt & Kinney 1996) or the  $H\alpha$  outflow ( $\sim 50^\circ$ ; Arribas & Mediavilla 1994). Therefore a different cause for this high velocity except motion in a nuclear potential appears to be unlikely. The extent of  $0.28''$  at  $PA 110^\circ$  translates into a radial distance of about 12 pc. Together with a velocity difference of  $\Delta v(12 \text{ pc}) \sim 75 \text{ km/s}$  (not corrected for inclination) this gives a lower limit

for the enclosed mass of about  $1.5 \times 10^7 M_{\odot}$ . This limit is in approximate agreement with the enclosed mass derived for the central black hole in NGC 3227 using  $H\beta$  reverberation mapping with a BLR size scale of  $\sim 17$  days and a FWHM of the  $H\beta$  line of 3900 km/s. With this technique Ho (1998) finds an enclosed mass of  $3.8 \times 10^7 M_{\odot}$  whereas Salamanca et al. (1994) and Winge et al. (1995) estimate a black hole mass of  $\sim 10^8 M_{\odot}$ .

### 4.3. The Rotation Curve

We derived rotation curves from the  $^{12}\text{CO}$  (1-0) and  $^{12}\text{CO}$  (2-1) data (using the routine 'ROTCUR' from GIPSY). This routine does not correct for the effect of beam smearing. However, as the peaks in the  $^{12}\text{CO}$  velocity fields occur at distances of about  $3.5''$  and the smallest beam has a FWHM of  $0.6''$  this should not affect radii below  $3.0''$  and outside the central  $1''$ . Using our  $^{12}\text{CO}$  measured values for the position of the dynamical center and a systemic velocity of  $v_{\text{sys}} = 1110 \pm 10$  km/s, we obtain  $i = (56 \pm 3)^\circ$  and  $PA = (160 \pm 2)^\circ$ , which are in excellent agreement with the values of Mundell et al. (1995b) derived from HI data.

To obtain a rotation curve ranging from the center to the outer HI disk ( $\sim 100''$ ) our  $^{12}\text{CO}$  rotation curve was combined with the HI data (Mundell et al. 1995b) from the literature (Fig. 7). To analyze our data we use two rotation curves: (1) For the *central 0.5''* we assumed Keplerian rotation in agreement with the enclosed mass estimates in the inner 25 pc until the velocities of the Keplerian curve dropped well below the  $^{12}\text{CO}$  velocities derived from the observations. (2) For the decomposition of the motion with the program 3DMod (see section 5) we extrapolated the rotation curve from its value at  $r = 0.5''$  to 0 km/s at  $r = 0.0''$ . Comparing this extrapolation of the rotation curve towards the center to the observed data allows us to find non-circular velocities associated with the nuclear region. This curve is referred to as our model rotation curve. Despite this difference the two rotation curves are basically identical for radii  $> 0.7''$ . Our  $^{12}\text{CO}$  data allows us to obtain a rotation curve for the range  $0.5'' < r \leq 5''$ . A rise of the rotation velocity till about  $3''$  to  $4''$  is observed. No reliable rotation curve measurements are available between  $r = 5''$  (end of the  $^{12}\text{CO}$  rotation curve) and  $r = 22''$  (innermost point of HI rotation curve not affected by beam smearing). To connect the  $^{12}\text{CO}$  curve with the HI curve we used a Keplerian velocity fall-off starting at  $r = 5''$ . For radii  $r > 22''$  the HI rotation curve was fully adopted.

In order to test the deduced rotation curve as well as the values for the inclination and position angle we looked for differences between the observed  $^{12}\text{CO}$  velocity field and a velocity field derived from the model rotation curve. In general the residuals (Fig. 8) in the difference field show characteristic patterns for mismatched parameters (see van der Kruit & Allen 1978). In our case they are less than about  $\pm 20$  km/s and indicate that most of the line emission can be described by the derived rotation curve satisfying the assumption of a simple rotating disk. An exception are the molecular bar and a region about  $1''$  south of the center that show residuals of  $\sim 35$  km/s.



#### 4.4. Dynamical Resonances

It is possible to estimate the position of the dynamical resonances from the rotation curve in conjunction with the bar length (Fig. 9). These resonances can be compared to the distribution of the molecular gas and the HII regions.

##### 4.4.1. Theoretical positions of resonances

NGC 3227 has probably a bar as indicated by optical and NIR observations (Mulchaey, Regan, Kundu 1997, De Robertis et al. 1998) with 6.7 kpc - 8.4 kpc radius and a position angle of about  $-20^\circ$  relative to the major kinematic axis. The presence of a bar is also supported by the locations of the HII regions (González Delgado & Perez 1998) that are consistent with a bar for radii  $\leq 50''$  (size of their field of view).

Under the assumption that the end of the bar is close to the corotation (CR) this gives an angular pattern speed of  $\Omega_p = (32 \pm 5)$  km/s, since the HI rotation curve (Mundell et al. 1995b) is relatively constant at these radii. The bar would have an ILR at  $r \sim 20''$  (1.7 kpc). At these distances one can find the SE-region of the  $^{12}\text{CO}$  line emission with two associated HII regions (Nr. 14 and 15, González Delgado & Perez 1998) as well as in northeast direction three more HII regions (Nr. 18 - 20). These  $^{12}\text{CO}$  emission line regions and the associated HII regions are consistent with the presence of an ILR.

However, the gas distribution and kinematics in the inner  $40''$  are not easily described by structures at the position of resonances due to the large-scale bar. Possible reasons for this are that the gas flow is disturbed due to interaction with NGC 3226, the HI cloud, or the HII regions. Another possibility is that the gas dynamics are just beginning to be influenced by the bar or that a stable semi equilibrium has not yet been reached. The analysis is hampered by the poor knowledge of the rotation curve for radii  $5'' < r < 22''$ .

### 5. DECOMPOSITION OF GAS MOTIONS IN NGC 3227

We were successful in decomposing the molecular gas motions in NGC 3227 in their circular and non-circular component using 3DMod with a model rotation curve (see section 4). The results of the decomposition are essential since they high-light complex non-circular features in the velocity field that will be modeled in section 7. 3DMod uses as an input the intensity map, the rotation curve and a velocity dispersion distribution to calculate the 3-dimensional spatial cubes of these properties. These spatial 3-dimensional cubes are rotated according to the inclination and position angle. Afterwards they are merged to a 3-dimensional  $xyv$  cube which can now be compared directly to the measured data cube. A detailed description of the decomposition algorithm used in 3DMod is given in Appendix A.

### 5.1. The Decomposition of the interferometric $^{12}\text{CO}$ data

The best decompositions were achieved using a systemic velocity of  $v_{sys} = 1110$  km/s in agreement with the derived rotation curve and visual inspection of the nuclear pv-diagrams. For the velocity dispersion a value of 30 km/s combined with a thin disk ( $0.2'' = 1$  resolution element) gave the best fit to the data. The decomposition shows that observed higher velocity dispersions are due to a spatial superposition of circular and non-circular components. The results are summarized in Table 2.

About 80 % of the total line emission in the inner  $8'' \times 8''$  of NGC 3227 is in excellent agreement with line emission from gas in circular motion. However, the decomposition of the  $^{12}\text{CO}$  (2-1) data reveals 3 distinct *components in non-circular motion*: the nuclear region, the molecular bar, and a  $\leq 0.6''$  knot  $1''$  south. The *nuclear region* accounts for 3% of the total flux in the inner  $8'' \times 8''$  and allows the following possible interpretations: **(1)** The velocity field of this component is in agreement with a counter rotating disk seen at a position angle of  $(41 \pm 3)$  km/s with an inclination of  $\sim 32^\circ$  and an axial ratio of  $\sim 0.85$ . At this inclination the nuclear disk is oriented orthogonal to the galaxy plane as  $|32^\circ| + |56^\circ| \approx 90^\circ$ . This disk is also responsible for most of the HCN(1-0) line emission (as in the case of NGC 1068 data ;Tacconi et al. 1997). **(2)** A different possible cause for the complex nuclear velocity field could be radial motions. However, such motions never change the direction of rotation on the major kinematic axis and can therefore be ruled out. **(3)** Further possibilities are motions in a bar potential or the warping of the molecular gas. We explore these issues further in section 7.

The *molecular bar* is about  $4''$  longer in the western direction than along its eastern extension and accounts for  $\sim 17\%$  of the CO line flux in the inner  $25'' \times 25''$ . The NS offset between the two sides of the bar might reflect its width. Its velocity is blue-shifted (on both sides of the nucleus) relative to the circular velocity by about 50 km/s.

## 6. MASS AND THICKNESS OF THE GAS DISK

A knowledge of the molecular gas mass and the dynamical mass of the nuclear region is required in order to estimate the thickness of the gas disk as well as the torques acting on it in the case of a possible warping (see section 7 and Appendix C). A comparison of the molecular gas mass to the dynamical mass of the nuclear region also shows that the molecular gas is a probe of the nuclear gravitational potential in NGC 3227 rather than providing a dominant component of it.

The molecular gas masses of the various component in the interferometric maps are given in Table 2. We used the  $\frac{N_{H_2}}{I_{CO}}$ -conversion factor of  $2 \times 10^{20} \frac{\text{cm}^{-2}}{\text{K km/s}}$  from Strong et al. (1989). (see e.g. Schinnerer, Eckart & Tacconi 1998 for discussion and references). In addition we estimated the dynamical mass by using the inclination corrected circular velocity for a given radius via  $M_{dyn}[M_\odot] = 232 \times v_{rot}(r)[\text{km/s}]^2 \times r[\text{pc}]$  .

The molecular gas contributes about 6 % to the dynamical mass in the inner 50 pc. We find

an average velocity dispersion  $\sigma_{obs} \approx 30 \text{ km/s}$  in the areas of the dispersion map ( $2^{nd}$ -order moment) that show circular motions. The velocity gradient of the rotation curve in the region from  $0.35''$  to  $2.0''$  is about  $68 \text{ km/s arcsec}^{-1}$ . This translates into an observed velocity spread with a  $FWHM_{rot}$  of  $\sim 41 \text{ km/s}$  for a beam of  $0.6''$ . The resulting velocity dispersion is  $\sigma_{rot} = \frac{FWHM_{rot}}{2/\sqrt{\ln(2)}} \approx 25 \text{ km/s}$ . We therefore find an intrinsic velocity dispersion  $\sigma_{real} \approx 17 \text{ km/s}$  in the inner  $6''$  of NGC 3227 using quadratic deconvolution. This implies that the symmetrical structures in the pv-diagrams that result in an increased apparent velocity dispersion have to be explained via a complex (ordered) velocity field rather than by an increased turbulence of the central molecular gas. Following the equations used in Schinnerer et al. (1999; see also Quillen et al. 1992, Combes & Bica 1997, Downes & Solomon 1998) we derive for the inner 550 pc a molecular gas disk height of about 15 pc.

## 7. RESULTS OF THE KINEMATIC MODELING

To analyze the complex kinematics in the inner 50 pc of NGC 3227 showing clear deviations from pure circular motions we modeled the data with 3DRings (see appendix B). 3DRings allows to model non-circular motions (1) via elliptical orbits with changing position angles characterizing gas motions in a bar and (2) via circular orbits leaving the plane of the galaxy representing a warp. The best bar solution fails to fully explain the data whereas the warp model gives a very satisfactory fit to the data.

The model subdivides the disk into many individual (circular or elliptical) orbits of molecular gas. The inclination, position angle and shape of the rotation curve for the overall galaxy were held fixed. Each fitting process was started at large radii and successively extended towards the center. In each case we tried several start set-ups that all converged to similar (best) solutions with mean deviations from the data of less than about  $10 \text{ km/s}$  and  $0.1''$  for each radius and velocity in the pv-diagrams and  $10^\circ$  in the position angle of the mapped structures. To test the quality and uniqueness of a model we used these criteria to derive the internal errors of the various model parameters ( $\alpha_0$ ,  $\xi \Delta t$ ,  $\omega(r)$  for the warp and  $\epsilon(r)$ ,  $PA(r)$  for the bar approach; see appendix B). For both approaches we used a rotation curve in which the motions of the inner few parsecs were assumed to be Keplerian due to the presence of an enclosed mass. The best results for the warp model is consistent with an enclosed mass of  $2 \times 10^7 M_\odot$ .

The pv-diagrams, the velocity field and the intensity map were used as a guidance during the fitting process. To allow for an easy comparison between the data and the models, we also displayed the pv-diagrams at an angular resolution of  $0.3''$  in order to enhance in the cleaned data the contrast of the small scale structures (Fig. 6). All source components in this representation of the data can also be identified in the images at the nominal angular resolution of  $0.6''$ .

### 7.1. The bar approach

Elliptical orbits caused by a bar potential are a generally accepted way to explain non-circular but well ordered motion in external galaxies in the presences of a bar potential. This is the only possibility to describe non-circular planar motion that is stable for several orbital time scales. However, high angular resolution NIR data shows no evidence for a strong nuclear bar (Schinnerer et al., in prep.). In Fig. 11 we show the curves for the position angle  $PA$  and an eccentricity  $\epsilon$  that describe the ellipses for our best fit in the framework of the bar approach. Fig. 12 shows that we are not able to account for the observed amount of counter rotation along the kinematic major axis and especially along  $PA\ 40^\circ$  close to the kinematic minor axis. Also, in all pv-diagrams the S-shape in the inner  $1''$  is not fully reproduced. However, the model fails completely to reproduce the pv-diagrams close to the kinematic minor axis, especially, the counter rotation observed at  $r \approx 0.5''$ . Also the fit can not explain the second flip with the velocity rising according to the enclosed central mass. The bar model can not fully reproduce the central  $1''$  intensity map and velocity field (Fig. 13) for this bar model.

Comparison to the calculated velocity fields and rotation curves of Wozniak & Pfenninger (1997) who used self-consistent models of barred galaxies shows that no strong apparent counter rotation along the minor axis is possible in such a scenario (their figure 5). This makes us confident that our bar approach is valid and that the bar scenario is a less likely solution for the central  $1''$  in NGC 3227.

### 7.2. The warp approach

Since the bar approach failed to fully explain the complex but well ordered motion in the inner  $1''$  of NGC 3227 we inspected the second possibility to explain non-circular motion: the warping of the gas disk mimicked by tilting circular orbits out of the plane of the galaxy. This approach seems reasonable as gas can leave the plane of the galaxy at the position of vertical resonances (Pfenninger 1984; Combes et al. 1990) and therefore probably populate the essential orbits. As warps have also been observed in accretion disks (e.g. NGC 4258 by Miyoshi et al. 1997) this seems a plausible way to pursue.

In Fig. 15 we show the excellent fit of our warp model to the pv-diagrams. The intensity map and velocity field of this model are shown in Fig. 16. The remaining differences (mainly reflecting the uneven intensity distribution in the data) are mostly due to the assumption of a uniform density distribution. The  $\omega(r)$  curve (Fig. 14) required to fit the data is remarkably smooth. The gas disk warps itself covering the nucleus starting from the south at  $r \sim 100$  pc ( $1.2''$ ). At  $r \sim 30$  pc ( $0.36''$ ) the warped disk is orthogonal to the host plane in agreement with the disk interpretation in section 5. At smaller radii the warp continues and the curvature becomes stronger. In this geometry the AGN is obscured at least ones.

The best fits result in  $\alpha_o = (-120 \pm 20)^\circ$  with respect to the major axis. The corresponding  $\xi \Delta t$  is  $(-2.7 \pm 0.7) \times 10^5 yrs$ . Therefore  $\sim 10$  rotations at  $r = 0.3''$  are required in order

to precess by  $360^\circ$ . For  $\xi\Delta t > 0$  an  $\alpha_o$  exist such that the resulting solution is identical in its kinematics. This indicates that there exists a single geometrical solution both with prograde and retrograde precession relative to the rotation of the host galaxy. To fit the counter rotation it is required that  $\omega(r)$  rises above  $90^\circ$ . This is in agreement with Pringle (1997) who has shown that in the case of accretion disks it is possible to obtain a stable warp till tilting angles of  $180^\circ$ .

### 7.3. Discussion of both approaches

The comparison of both best solutions shows that the warp model is a much better and preferred description of the data. The greatest shortcoming of the planar bar model is that it fails to reproduce the counter rotation along the minor axis, although the fit is satisfying along the kinematic major axis. As a strong stellar bar is not observed in the NIR (Chapman et al. (1999) and our SHARP K-band speckle image reconstructions) strong streaming motions can not be evoked to explain the remaining differences between the bar model and the data. These facts combined with the poor fit to the kinematic minor axis  $pv$ -diagram and to the observed spectra (Fig. 17) makes it not straight forward to explain the kinematics in the inner  $0.8''$  with a bar, i.e. via a pure planar system with ordered (elliptical) orbits. Therefore our modeling suggest that the molecular nuclear gas disk in NGC 3227 is likely to be warped in the inner 70 pc. Also it is indicated that the gas observed at radii  $\geq 13$  pc is relatively uniformly distributed rather than constrained to some distinct areas in the nuclear region.

The warp approach results in a very good fit to the  $xyv$  data cube (see also spectra in Fig. 17) and therefore we definitely favor this model. Theoretical analyses of the bulge formation and the bar dissolution using orbit calculations or N-body simulations show that with a sufficient central mass density 3-dimensional stellar orbits form that can support and enhance the so-called boxy or peanut appearance of bulges. The interesting zone is the region where the bar potential is only as strong as the bulge potential of the central mass. This happens often at about the distance of the radial ILR. Then in addition to the radial ILR a inner vertical resonance (IVR) forms which allows stars to leave the plane of the disk (Pfenniger 1984, Combes et al. 1990). Friedli & Benz (1993) have shown that even well within the plane of a barred galaxy vertical resonances can be high-lighted by the gas being pushed out of the plane. Since  $x_4$  orbits are vertically unstable, the gas can leave the plane very quickly after formation of the bar and becomes trapped in stable anomalous orbits inclined with respect to the major axis  $x$  ( $ANO_x$  orbits, see Pfenniger & Friedli 1991). Similarly Garcia-Burillo et al. (1999) observe in the warped galaxy NGC 4013 substantial amounts of molecular gas well above the plane. In this case, however, the star formation activity in the disk might be responsible. For NGC 3227 (and NGC 1068, Schinnerer et al. 1999) we find that the gas disk starts to warp at a radius at which the bulge begins to dominate the gravitational potential. Once out of the plane, the gas would be mainly supported by the potential of the bulge, competing with that of the bar or disk. As the

gas is dissipative compared to the stars it is valid to assume that it will stay on ordered non-crossing orbits which will strongly favor the formation of warps.

In order to move the gas out of the plane a torque is needed. Torques can be induced by a non-spherical galactic potential (similar to the effect of the halo on the HI disk), by the radiation pressure of the radio jet (similar to the central radiation source causing the warp in the accretion disk; Pringle 1996, 1997), by gas pressure in the ionization cone (Quillen & Bower 1999) or as a transient phenomenon by the gravitational force of a dislocated molecular cloud complex (see also appendix C for a more detailed discussion). Estimates of these effects in the nuclear region of NGC 3227 (see table in appendix) show that torques induced by gas pressure or GMCs are the two most likely causes.

The only worrying aspect of the warp model is seen in the 3-dimensional view (see Fig. 18). The direct view onto the AGN is seemingly blocked by the warped gas disk. This is in contradiction to the unified scheme for Seyfert galaxies that proposes for Seyfert 1 types a clear view to the central engine. This problem can be softened, if the orbits are not homogeneously filled with molecular gas but rather with molecular clumps smaller than the size of the Seyfert 1 nucleus. In this case no effective shadowing of the compact Seyfert nucleus itself can occur.

The interpretation of the X-ray data demands a warm absorber which would be located in the immediate vicinity of the AGN (Komossa & Fink 1997). Recent observations of absorption lines in the UV of Seyfert 1 galaxies show that these absorptions occur in galaxies with a warm absorber (as NGC 3227; Crenshaw et al. 1999) at larger radial distances than the BLR.

The different classifications as a Seyfert 2 or Seyfert 1 found for NGC 3227 in the literature are most likely caused by variability. NGC 3227 was first classified as a Seyfert 2 by Khachikian & Weedman (1974). However, from data with higher S/N Osterbrock (1977) identified it as a Seyfert 1.2. Further measurements by Heckman et al. (1981) and Peterson et al. (1982) confirmed this classification. On the other hand Schmidt & Miller (1985) note that the general low (and variable) strength of the emission line spectrum is in better agreement with a Seyfert 2 nucleus. This indicates that the nucleus of NGC 3227 is either intrinsically relatively weak for a Seyfert 1 galaxy or it is weakened by obscuration. Obscuring gas in the warped molecular disk may well be responsible for the observed variability and varying classification of the nuclear source in NGC 3227.

It is also possible to compare the warp model with results from optical polarimetry. Thompson et al. (1980) as well as Schmidt & Miller (1985) have observed a polarization of about  $\sim 1\%$  for the continuum as well as the permitted and forbidden emission lines of the BLR and NLR. The degree and position angle of the polarization for the continuum and the emission lines are similarly implying a common cause for the polarization. The position angle ( $131^\circ \pm 8^\circ$ ) of the polarization is not in agreement with the galactic major axis or the

axis of the radio jet but it is in agreement with the apparent enhancement of disk material due to projection effects in the warp geometry as proposed here.

*The described circumstances provide a strong independent support both for the presence of material on the line sight to the nucleus as well as for the particular warp geometry we obtained by analyzing the kinematics of the molecular gas.*

## 8. SUMMARY AND IMPLICATIONS

1. *Molecular gas close to the nucleus.*— We obtained PdBI data of the HCN(1-0) and the  $^{12}\text{CO}$  line emission of the nuclear region in NGC 3227 with sub-arcsecond spatial resolution. These data allow for the first time a detailed and quantitative analysis of the molecular gas kinematics in the inner 500 pc of this Seyfert 1 galaxy. NGC 3227 shows a nuclear gas ring with a diameter of about 250 pc similar to the one observed in NGC 1068 (Tacconi et al. 1997, Schinnerer et al. 1999).

Gas emission at a radius of about 13 pc is detected in the  $^{12}\text{CO}$  (2-1) line emission in NGC 3227. This emission shows a remarkable velocity offset to the systemic velocity and allows for the first time to use the molecular line emission for an estimation of the enclosed mass in the inner 25 pc of about  $\sim 1.5 \times 10^7 M_{\odot}$  (not correcting for inclination effects). This is in agreement with estimates from other wavelength ranges.

2. *The HCN(1-0) line emission is very concentrated.*— Comparison between the HCN(1-0) and the  $^{12}\text{CO}$  data to single dish observations suggest that the  $^{12}\text{CO}$  line emission is distributed in a disk of FWHM  $\sim 25''$  whereas the HCN(1-0) line emission is concentrated on the nucleus. The direct comparison to our high resolution interferometric  $^{12}\text{CO}$  (2-1) data furthermore suggests that the HCN(1-0) is mainly arising from a region of size  $\leq 0.6''$  which shows unusual kinematical behavior.

3. *The nuclear molecular gas disk is likely to be warped.*— To model the nuclear kinematics in NGC 3227 observed in the  $^{12}\text{CO}$  (2-1) line emission we used a modified tilted ring model which is able to describe gas motions in a thin ( $\sim 17$  pc), warp disk as well as in a bar potential. Our modeling of the nuclear kinematics with 3DRings suggests that a warped gas disk provides a better explanation to the observed gas motions than motion evoked by a bar potential. The warp of the gas disk starts at an outer radius of  $\sim 75$  pc and is perpendicular to the outer disk of the host at  $\sim 30$  pc. This warping indicates an obscuration of the nucleus at small radii by a thin gas disk. This is in agreement with findings at other wavelengths which suggest an obscuration at radii larger than the BLR, including parts of the NLR. The most likely cause for the warping of the gas disk is the gas pressure in the ionized gas cones as traced by the NLR. This pressure results in a torque onto the gas disk. This mechanism was recently also discussed by Quillen & Bower (1999) as a possible cause for the warp in M 84.

4. *Small molecular gas tori are not needed.*— Our observations of NGC 1068 (Schinnerer et al. 1999) and NGC 3227 suggest that warps of the circumnuclear gas disk may be common. Even though nothing in our observations can rule out the existence of small molecular tori with radii  $\leq 25$  pc our finding implies that not under all circumstances the postulated molecular gas torus of most unified schemes for Seyfert galaxies are required to obscure the nuclei. A somewhat peculiar distribution of molecular gas or dust in the host galaxy as proposed e.g. by Malkan et al. (1998) appears to be more likely. However, the obscuring gas and dust may still be in well ordered motion.

*Acknowledgments:* IRAM is financed by INSU/CNRS (France), MPG (Germany) and IGN (Spain). We thank the staff on Plateau de Bure for doing the observing, and the staff at IRAM Grenoble for help with the data reduction, especially D. Downes, R. Neri and J. Wink. For fruitful discussions we thank A. Baker, D. Downes, P. Englmaier, J. Gallimore, O. Gerhard, R. Maiolino, A. Quillen, N. Scoville and L. Sparke. We used the NASA/IPAC Extragalactic Database (NED) maintained by the Jet Propulsion Laboratory, California Institute of Technology, under contract with the National Aeronautics and Space Administration.



## REFERENCES

- Antonucci, R. R. J. 1993, *ARA&A*, 31, 473
- Arnaboldi, M., Sparke, L.S., 1994, *A. J.*, 107, 958.
- Arribas, S., Mediavilla, E., 1994, *Ap. J.*, 437, 149.
- Athanassoula, E., 1992a, *M.N.R.A.S.*, 259, 328.
- Athanassoula, E., 1992b, *M.N.R.A.S.*, 259, 345.
- Binney, J., 1992, *Ann.Rev.Astr.Ap.*, 30, 51.
- Blitz, L., Mathieu, R.D., Bally, J., 1986, *Ap. J.*, 311, 142.
- Blundell, R., Gundlach, K.H., Blum, E.J., Ibrügger, J. and Hein, H., 1985, in *Int. Symposium on Millimeter and Submillimeter Radio Astronomy*, URSI, Granada, p. 117
- Blundell, R., Carter, M. and Gundlach, K.H., 1988, *Int. Journ. Infrared and Millimeter Waves*, 9, 361
- Braine, J., Combes, F., 1992, *Astron. Astrophys.*, 264, 433.
- Braine, J., Combes, F., Casoli, F., Dupraz, C., Gérin, M., Klein, U., Wielebinski, R., Brouillet, N., 1993, *Astron. Astrophys. Suppl.*, 97, 887.
- Cameron, M., et al. 1993, *Ap. J.*, 419, 136 .
- Chapman, S.C., Morris, S.L., Walker, G.A.H., 1999, *Proceedings of 'Science with Adaptive Optics'*, Garching, Germany, in press
- Clements, E.D., 1981, *M.N.R.A.S.*, 197, 829.
- Combes, F., Becquaert, J-F., 1997, *Astron. Astrophys.*, 326, 554.
- Combes, F., Debbasch, F., Friedli, D., Pfenniger, D., 1990, *Astron. Astrophys.*, 233, 82.
- Contopoulos, G., Papayannopoulos, Th., 1980, *Astron. Astrophys.*, 92, 33.
- Crenshaw, D.M., Kraemer, S.B., Boggess, A., Maran, A.P., Mushotzky, R.F., Wu, C.-C., 1999, *Ap. J.*, 516, 750.
- De Robertis, M.M., Hayhoe, K., Yee, H.K.C., 1998, *Ap. J. Supp.*, 115, 163.
- De Vaucouleurs, G., 1975, *Stars and Stellar Systems*, Vol. 9, University of Chicago Press, p. 557
- Dickel, J.R., 1976, in *Methods of experimental Physics*, Part 12c, ed. M. Marton, Academic Press, New York, San Francisco
- Downes, D., Solomon, 1998, submitted
- Edelson, R., & Malkan, M. A. 1987, *Ap. J.*, 323, 516.
- Friedli, D., Benz, W., 1993, *Astron. Astrophys.*, 268, 65.
- Gallimore, J.F., Baum, S.A., O'Dea, C.P., 1997, *Astrophys. and Space Science* 248, 253.
- Garcia, A.M., 1993, *Astron. Astrophys. Suppl.*, 100, 47.
- Garcia-Burillo, S., Combes, F., Neri, R., 1999, *Astron. Astrophys.*, 343, 740.
- Goldstein, H., 1980, *Classical Mechanics*, 2nd edition, Reading: Allison Wesley

- González Delgado, R.M., Perez, E., 1997, M.N.R.A.S., 284, 931.
- Heckman, T.M., Miley, G.K., van Breugel, W.J.M., Butcher, H.R., 1981, Ap. J., 247, 403.
- Ho, L.C., 1998, Invited review to "Observational Evidence for Black Holes in the Universe", ed. S.K. Chakrabarti (Dordrecht: Kluwer), in press)
- Keel, W.C., 1996, Ap. J. Supp., 106, 27.
- Khachikian, E.Y., Weedman, D.W., 1974, Ap. J., 192, 581.
- Komossa, S., Fink, H., 1997, Astron. Astrophys., 327, 483.
- Lovelace, R.V.E., 1998, Astron. Astrophys., 338, 819.
- Maiolino, R., Ruiz, M., Rieke, G.H., Keller, L.D., 1995, Ap. J., 446, 561.
- Maiolino, R., Ruiz, M., Rieke, G.H., Papadopoulos, P., 1997, Ap. J., 485, 552.
- Malkan, M.A., Gorjian, V., Tam, R., 1998, Ap. J. Supp., 117, 25.
- Martini, P., Pogge, R.W., 1999, A. J., in, press.
- Meisenheimer, K., Roeser, H.-J., Schloetelburg, M., 1996, Astron. Astrophys., 307, 61.
- Meixner, M., Puchalsky, R., Blitz, L., Wright, M., Heckman, T., 1990, Ap. J., 354, 158.
- Mestel, L., 1963, M.N.R.A.S., 126, 553.
- Miyoshi, M., Moran, J., Herrnstein, J., Greenhill, L., Nakai, N., Diamond, P., Inoue, M., 1995, Nature, 373, 127
- Mulchaey, J.S., Regan, M.W., Kunu, A., 1997, Ap. J. Supp., 110, 229.
- Mundell, C.G., Holloway, A.J., Pedlar, A., Meaburn, J., Kukula, M.J., Axon, D.J., 1995a, M.N.R.A.S., 275, 67.
- Mundell, C.G., Pedlar, A., Axon, D.J., Meaburn, J., Unger, S.W., 1995b, M.N.R.A.S., 277, 641.
- Nicholson, R.A., Bland-Hawthorn, J., Taylor, K., 1992, Ap. J., 387, 503.
- Osterbrock, D.E., 1977, Ap. J., 215, 733.
- Papadopoulos, P.P., Seaquist, E.R., 1998, Ap. J., 492, 521.
- Peterson, B., 1997, An Introduction to Active Galactic Nuclei, Cambridge, Cambridge Univ. Press
- Peterson, B.M., Foltz, G.B., Byard, P.L., Wagner, R.M., 1982, Ap. J. Supp., 49, 469.
- Pfenniger, D., 1984, Astron. Astrophys., 134, 373.
- Pfenniger, D., Friedli, D., 1991, Astron. Astrophys., 252, 75.
- Pier, E. A., & Krolik, J. H. 1992, Ap. J., 401, 99 .
- Pier, E. A., & Krolik, J. H. 1993, Ap. J., 418, 673.
- Pringle, J.E., 1996, M.N.R.A.S., 281, 357.
- Pringle, J.E., 1997, M.N.R.A.S., 292, 136.
- Quillen, A.C. & Bower, G.A., 1999, submitted to Ap. J., astro-ph/9812312
- Quillen, A.C., De Zeeuw, P.T., Phinney, E.S., Phillips, T.G., 1992, Ap. J., 391, 121.
- Regan, M.W., Mulchaey, J.S., 1999, A. J., in press, .

- Rogstad, D.H., Lockhart, I.A., Wright, M.C.H., 1974, *Ap. J.*, 193, 309.
- Rubin, V.C., Ford, W.K. 1968, *Ap. J.*, 154, 431.
- Salamanca, I. et al., 1994, *Astron. Astrophys.*, 282, 742.
- Schinnerer, E., Eckart, A., Tacconi, L.J., 1998, *Ap. J.*, 500, 147.
- Schmidt, G.D., Miller, J.S., 1985, *Ap. J.*, 290, 517.
- Schmitt, H.R., Kinney, A.L., 1996, *Ap. J.*, 463, 498.
- Schwarz, U.J., 1985, *Astron. Astrophys.*, 142, 273.
- Shlosman, I., Frank, J., Begelman, M.C., 1989, *Nature*, 338, 45
- Sparke, L.S., 1996, *Ap. J.*, 473, 810.
- Stacey, F.D., 1969, 'Physics of the Earth', Space Science Text Series, J. Wiley & sons Inc.
- Strong, A. W., et al. 1987, *Proc. 20th Intern. Cosmic Ray Conf.*, I, 125
- Tacconi, L.J., Gallimore, J.F., Genzel, R., Schinnerer, E., Downes, D., 1997, *Astrophys. and Space Science* 248, 59.
- Telesco, C.M., Decher, R., 1988, *Ap. J.*, 334, 573.
- Thompson, I., Landstreet, J.D., Stockman, H.S., Angel, J.R.P., Beaver, E.A., 1980, *M.N.R.A.S.*, 192, 53.
- Ulvestad, J.S., Wilson, A.S., Sramek, R.A., 1981, *Ap. J.*, 247, 419.
- van der Kruit, P. C., Allen, R. J., 1978, *Ann.Rev.Astr.Ap.*, 16, 103.
- Wild, W., 1995, "The 30 m Manual", IRAM
- Winge, C., Peterson, B.M., Horne, K., Pogge, R.W., Pastoriza, M.G., Storchi-Bergmann, T., 1995, *Ap. J.*, 445, 680.
- Wozniak, H., Pfenniger, D., 1997, *Astron. Astrophys.*, 317, 14.

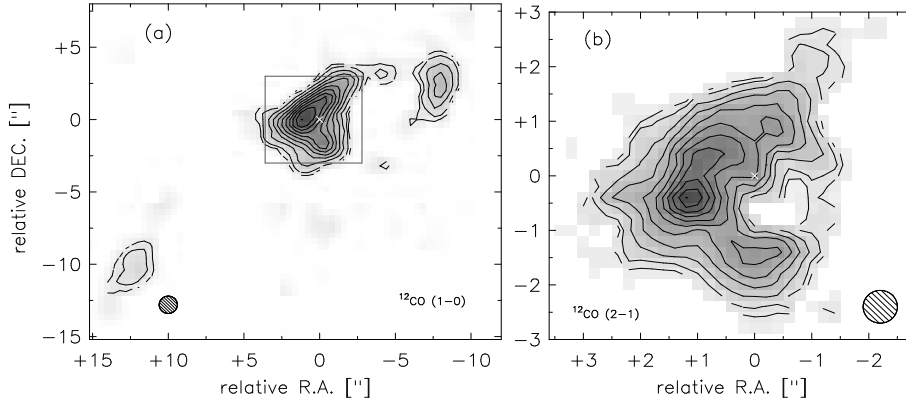


Fig. 1.— The IRAM PdBI maps of NGC 3227. The intensity maps ( $0^{th}$ -order moment) of the  $^{12}\text{CO}$  (1-0) line emission (left) at a resolution of  $1.2''$  and in contours of 5, 10, 20, ... 100 % of the maximum of  $8.78 \text{ Jy/beam km/s}$ . The indicated area corresponds to the  $^{12}\text{CO}$  (2-1) map show in the right panel. The contours of the  $^{12}\text{CO}$  (2-1) map at a resolution of  $0.6''$  are in 5, 10, 20, ... 100% of the peak of  $9.18 \text{ Jy/beam km/s}$ . The  $^{12}\text{CO}$  (1-0) map contains only about 20% of the intensity of the IRAM 30 m map whereas the  $^{12}\text{CO}$  (2-1) map contains about 10% of the total line intensity of the 30 m map.

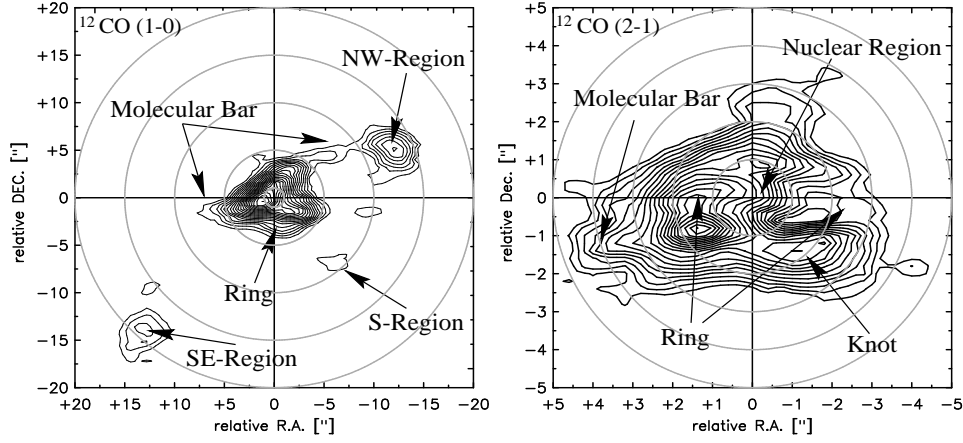


Fig. 2.— The de-projected maps of the PdBI  $^{12}\text{CO}$  line emission. The maps are de-projected by correcting for an inclination angle of  $i=56^\circ$  and a position angle of  $PA=158^\circ$ . To ease the comparison to the real data the blue side of the major kinematic axis was aligned to the north. The contours are 5, 10, 15, 20, ... 100% of the peak intensity. The regions discussed in the text are indicated.

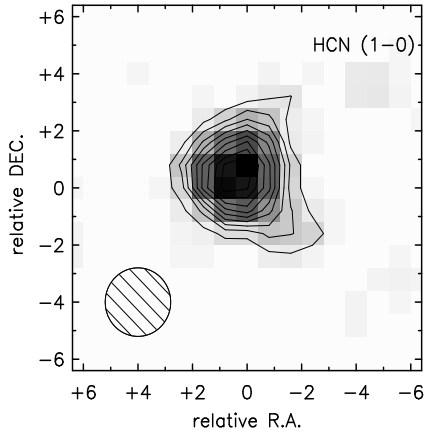


Fig. 3.— IRAM PdBI map of the HCN(1-0) line emission in NGC 3227 at a resolution of  $2.4''$ . The contours are 30, 40, ... 100% of the peak of 1.93 Jy/beam km/s.

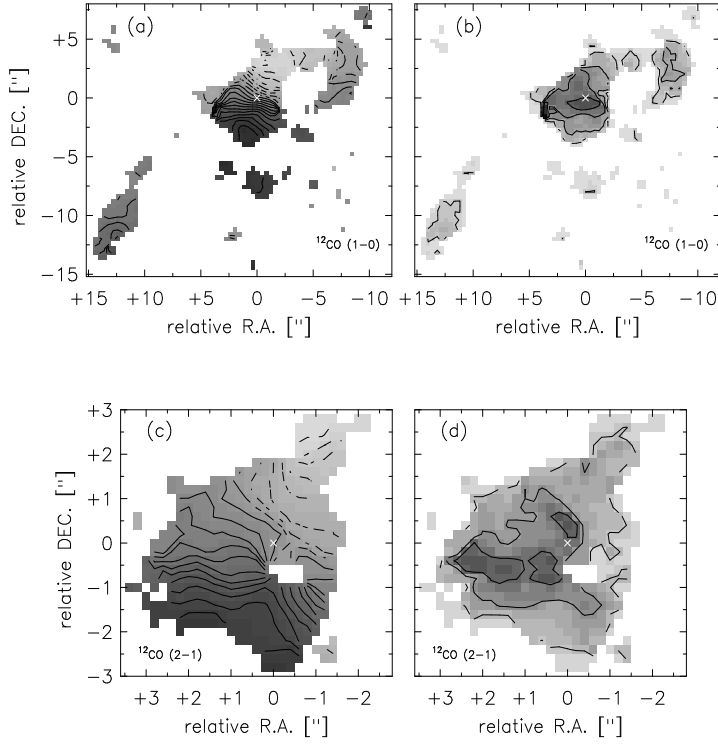


Fig. 4.— Velocity field and map of the velocity dispersion in NGC 3227 as obtained from the  $^{12}\text{CO}$  (1-0) line emission (a and b) and of the  $^{12}\text{CO}$  (2-1) line emission (c and d). The contours are at velocities of -220, -200, ... 160 km/s whereas the first solid line corresponds to  $\approx 1094$  km/s close to the systemic velocity of  $v_{\text{sys}} = 1110$  km/s. The contours in the velocity dispersion maps are at 15, 30, 45 and 60 km/s, respectively.

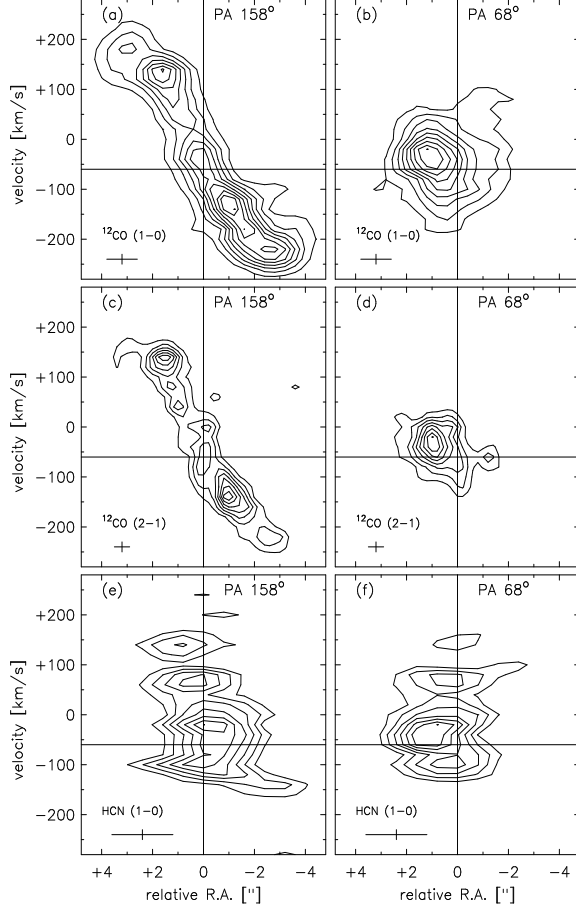


Fig. 5.— pv-diagrams in NGC 3227 taken along the major and minor kinematic axis of the  $^{12}\text{CO}$  (1-0) line emission (a and b) and the  $^{12}\text{CO}$  (2-1) line emission (c and d). The contours are 20, 30, ... 100% of the peak of the  $^{12}\text{CO}$  (1-0) emission and 30, 40, 100% of the peak of the  $^{12}\text{CO}$  (2-1) emission. pv-diagrams of the HCN(1-0) line emission (e and f) in NGC 3227 along the major and minor kinematic axis. The contours are in 40, 50, ... 100% of the peak intensity.



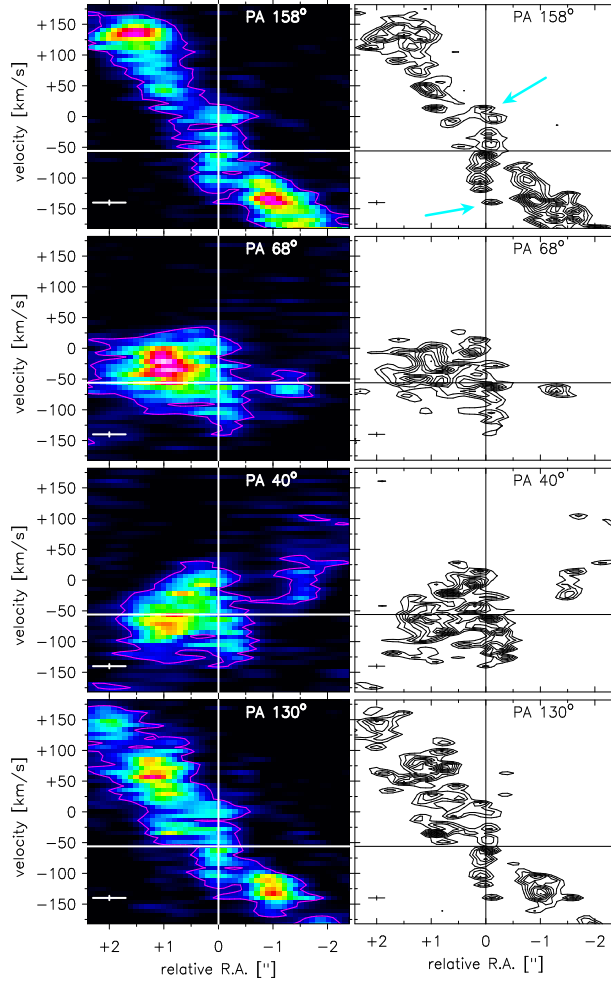


Fig. 6.— pv-diagrams of the nuclear  $^{12}\text{CO}$  (2-1) line emission in NGC 3227 along different position angles. In all pv-diagrams the fast change of the velocity inside the inner  $1''$  is clearly visible as an S-shape. To highlight this complex velocity behavior the data is also shown at a nominal resolution of  $0.3''$  (right). For comparison the corresponding pv-diagrams at the achieved instrumental resolution of  $0.6''$  are shown in color on the left panels. The (magenta) contour corresponds to  $3\sigma$ , with  $1\sigma = 6.2 \text{ mJy/beam}$  at a spectral resolution of  $7 \text{ km/s}$ . For the first time seen in the molecular gas emission the data show a rising rotation curve towards smaller radii with the extreme velocities (indicated by arrows) at radial separations of  $\approx 0.15''$  ( $13 \text{ pc}$ ) indicating an enclosed mass of  $\geq 2 \times 10^7 M_{\odot}$ , not correcting for inclination effects. This value is consistent with  $\sim 10^8 M_{\odot}$  estimated from  $\text{H}\beta$ -reverberations mapping by Salamanca et al. (1994).

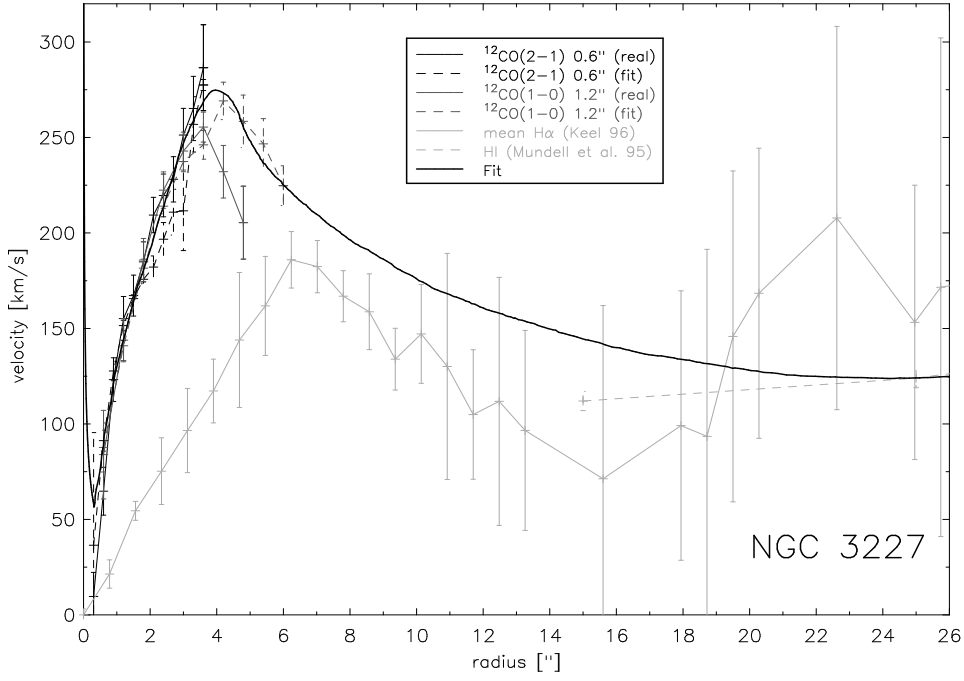


Fig. 7.— The rotation curves of NGC 3227. The rotation curves derived from the  $^{12}\text{CO}$  data as well as curves taken from the literature are shown. The thick line is the best fit to the different curves.

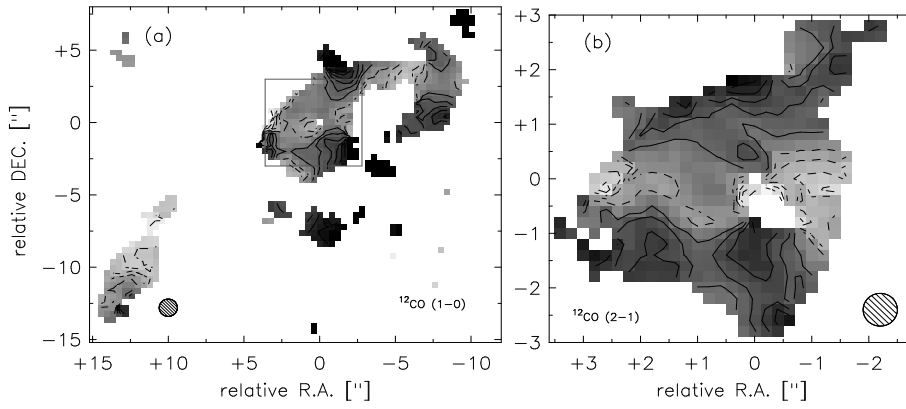


Fig. 8.— Residuals of the fit to the velocity field in NGC 3227 of the  $^{12}\text{CO}$  (1-0) line emission (left) and the  $^{12}\text{CO}$  (2-1) line emission (right). Positive residuals are shown in solid contours starting at 10 km/s in steps of 10 km/s, negative residuals start at -10 km/s.

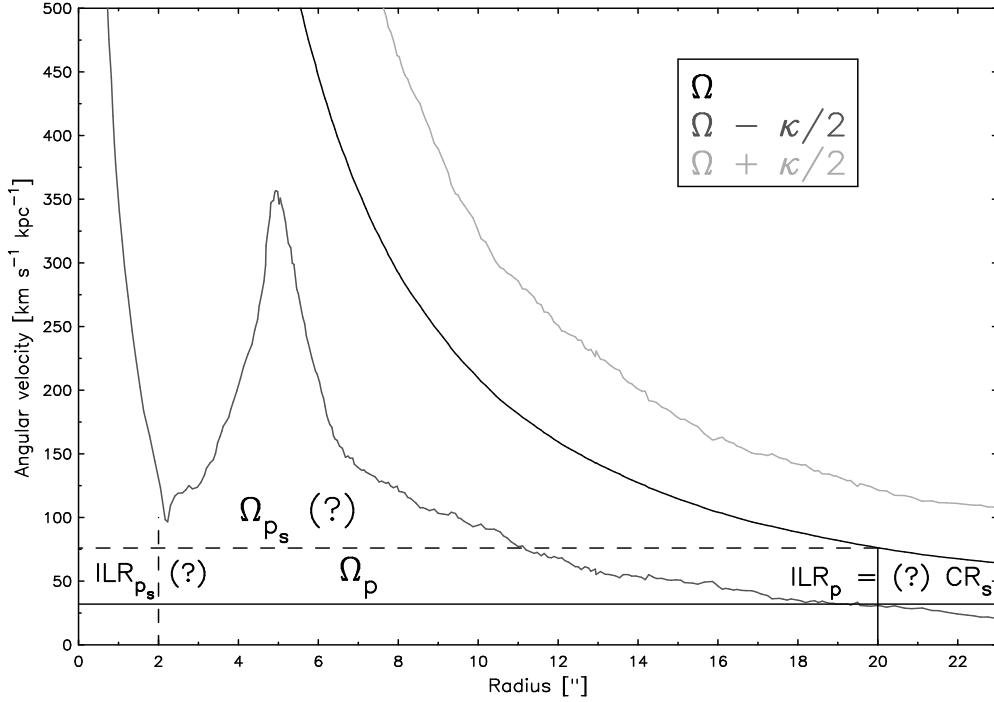


Fig. 9.— Dynamical resonances in NGC 3227. The angular velocity  $\Omega$  as well as the  $\Omega + \frac{\kappa}{2}$  and  $\Omega - \frac{\kappa}{2}$  curves are shown. The (primary) outer bar has an angular pattern velocity  $\Omega_{p_p}$  indicating an  $\text{ILR}_p$  at about  $r=20''$ . The resulting angular velocity for a possible (secondary) inner bar  $\Omega_{p_s}$  as well as its related  $\text{ILR}_s$  are uncertain and therefore labeled with a question mark. For further explanations see text.

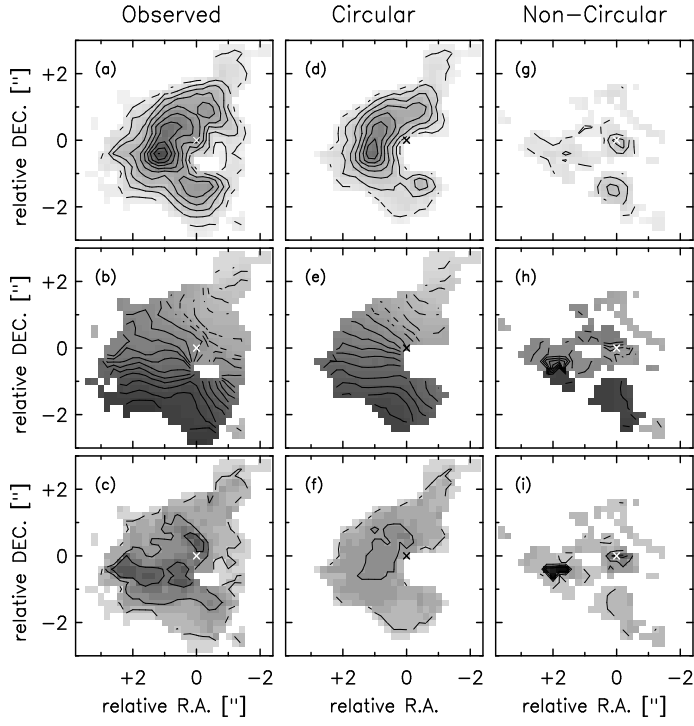


Fig. 10.— Decomposition of the  $^{12}\text{CO}$  (2-1) data ( $a - c$ ) into components that follow pure circular motion ( $d - f$ ) and those that follow non-circular motion ( $g - i$ ) in NGC 3227. The contours of the intensity maps ( $a, d, g$ ) are in 10, 20, ... 100% of the peak intensity in the observed map. In the velocity fields ( $b, e, h$ ) the contours are shown from -220 km/s till -80 km/s (broken line) and from -60 km/s till 160 km/s (solid line) in steps of 20 km/s. The contours of the velocity dispersion maps ( $c, f, i$ ) are at 15, 30, 45 and 60 km/s.

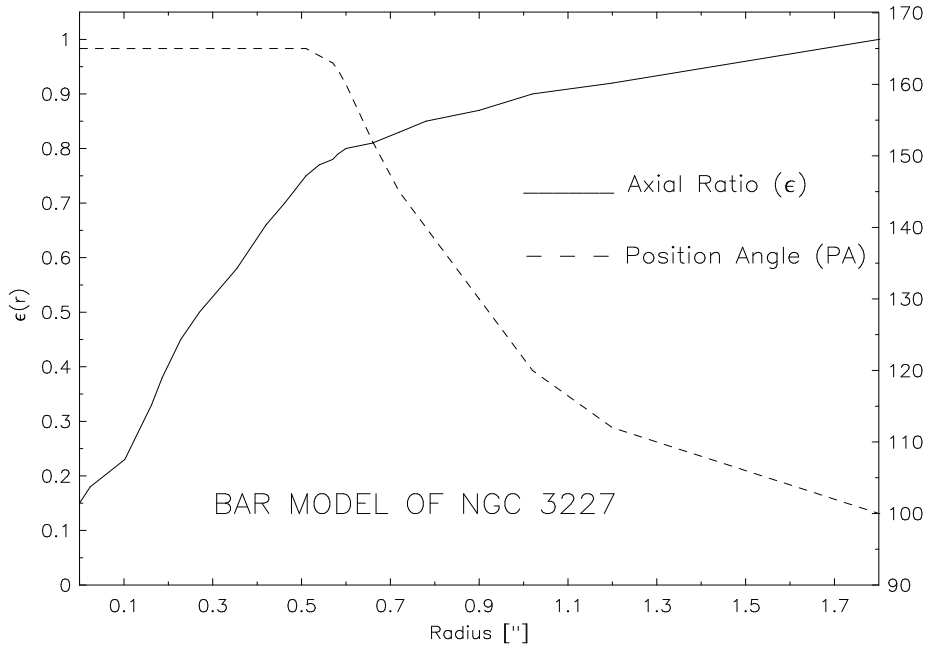


Fig. 11.— The curves of the position angle  $PA$  and eccentricity  $\epsilon$  of the bar approach in NGC 3227. The  $\epsilon$  curve (solid line) and the  $PA$  curve (broken line) for the best bar model.

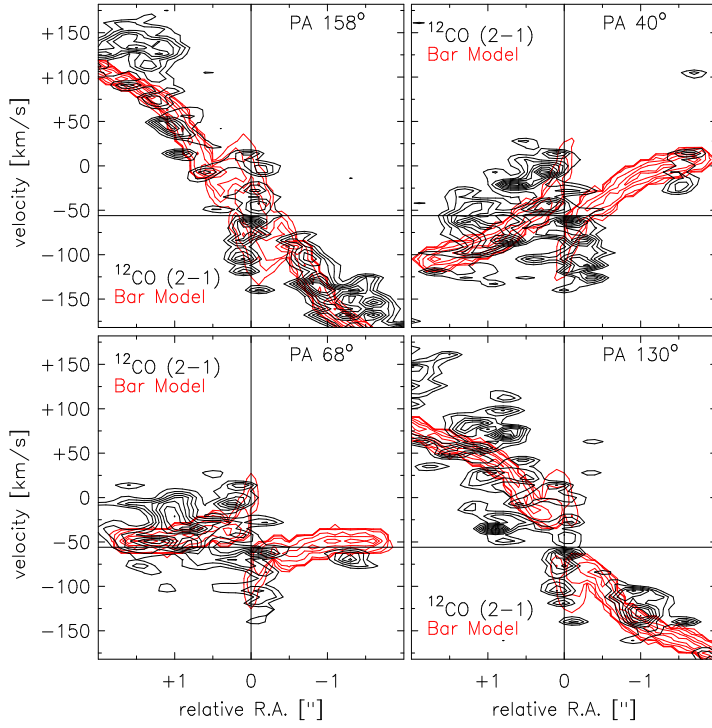


Fig. 12.— pv-diagrams for the bar approach in NGC 3227. The data (black contours) along different position angles are shown together with the results (red contours) of the bar model. To highlight the complex velocity behavior the data is shown at a nominal resolution of  $0.3''$ . In the pv-diagram at a resolution of  $0.6''$  the lowest contour corresponds to  $3\sigma$ , with  $1\sigma = 6.2$  mJy/beam at a spectral resolution of 7 km/s.

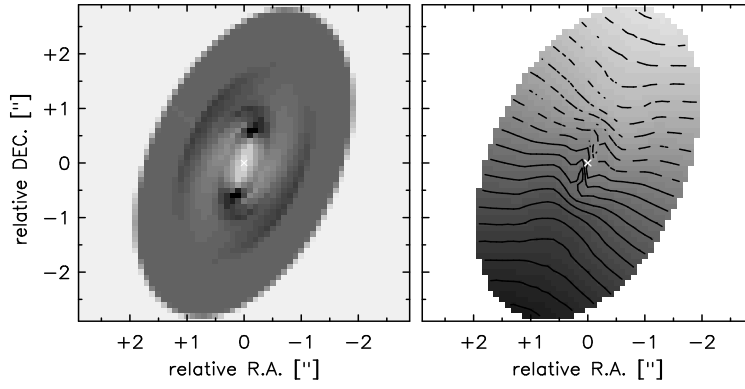


Fig. 13.— Intensity map (left) and velocity field (right) of the bar approach in NGC 3227. The contours of the velocity field range from -200 km/s to 200 km/s in steps of 20 km/s. The negative velocities are indicated by broken lines.



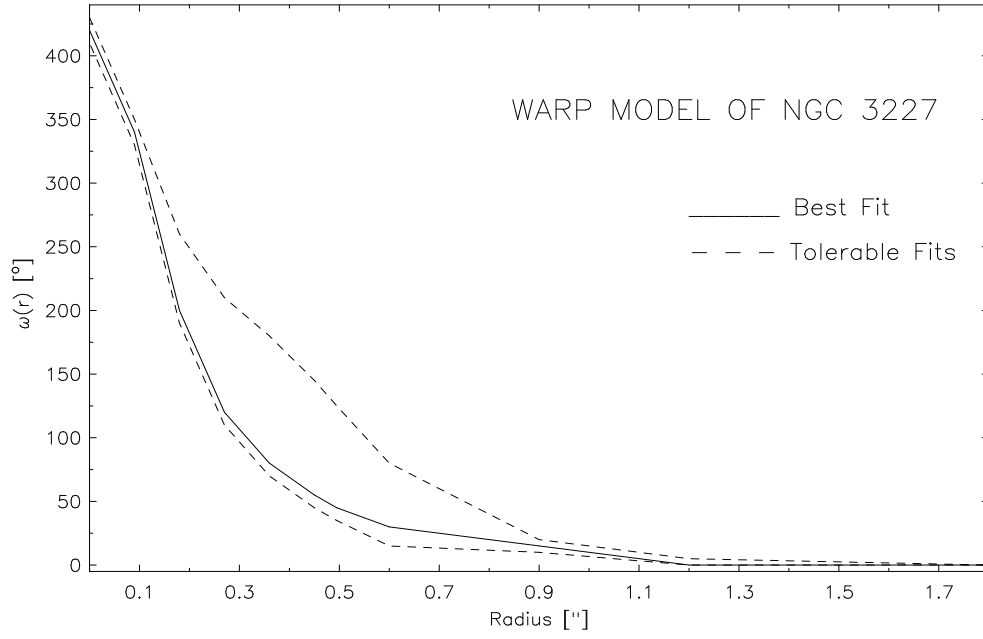


Fig. 14.— The  $\omega(r)$  curve of the warp approach in NGC 3227. The solid line represents the best fit to the data. The broken lines indicate the range over which satisfying fits to the data are still possible.

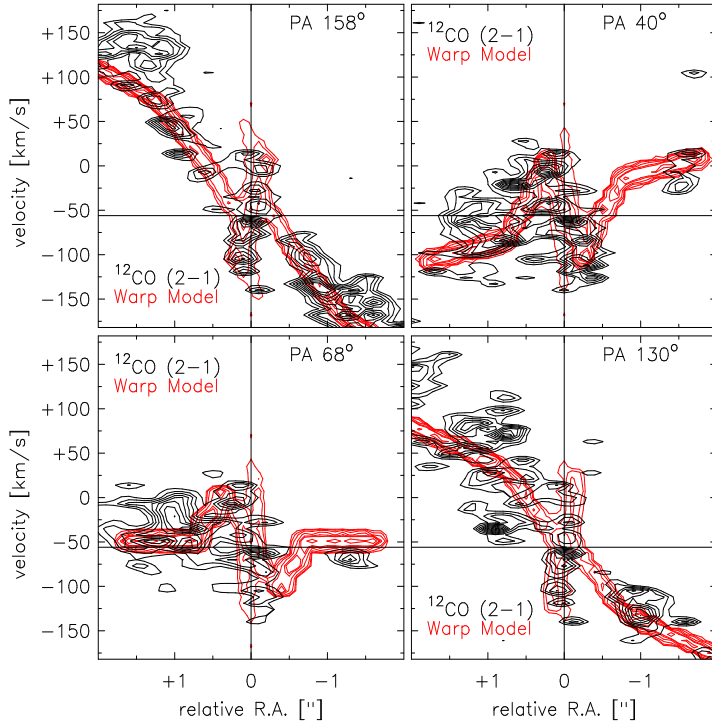


Fig. 15.— pv-diagrams for the warp approach in NGC 3227. The data (black contours) along different position angles are shown together with the results (red contours) of the warp model. To highlight the complex velocity behavior the data is shown at a nominal resolution of  $0.3''$ . In the pv-diagram at a resolution of  $0.6''$  the lowest contour corresponds to  $3\sigma$ , with  $1\sigma = 6.2$  mJy/beam at a spectral resolution of 7 km/s.

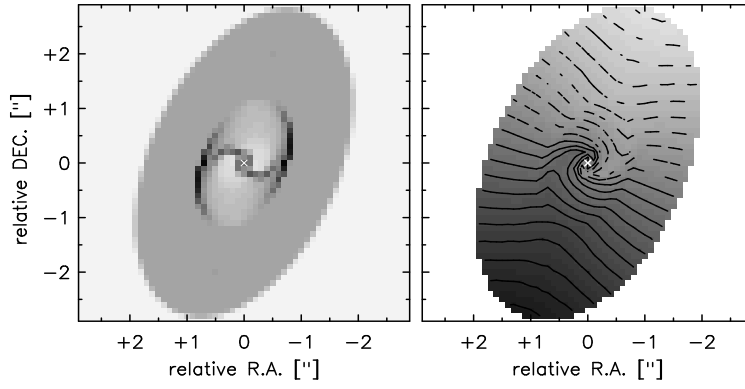


Fig. 16.— Intensity map (left) and velocity field (right) of the warp approach in NGC 3227. The contours of the velocity field range from -200 km/s to 200 km/s in steps of 20 km/s. The negative velocities are indicated by broken lines.

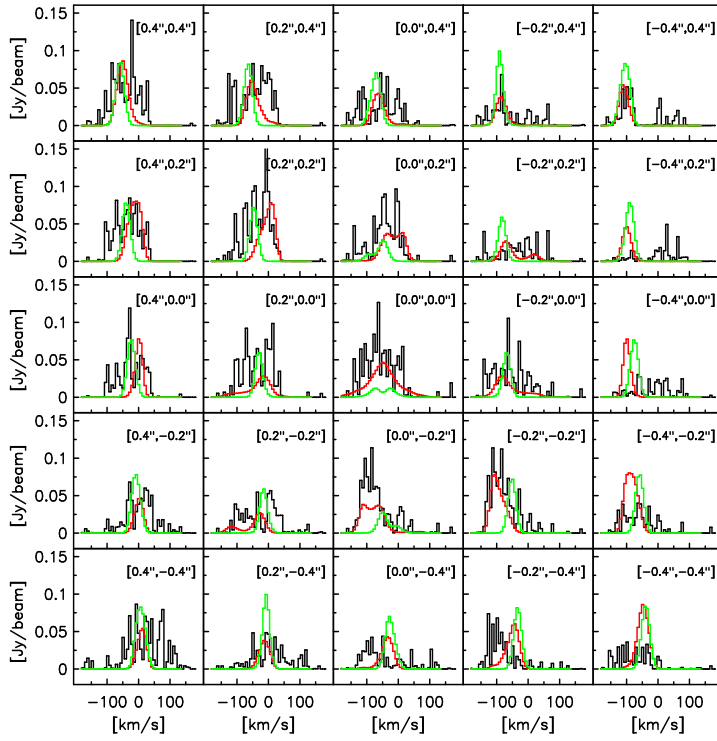


Fig. 17.— Here we show a comparison of the measured spectra (black) and the spectra given by the warp (red) and bar model (green). We concentrate on the central  $0.8'' \times 0.8''$  in steps of  $0.2''$ . The warp model represents an acceptable fit to the observed data that reflect the complex velocity field. The agreement of the bar model with the data is not as good as it cannot reproduce the asymmetric line shapes especially at positions north-east and south-west of the nucleus.

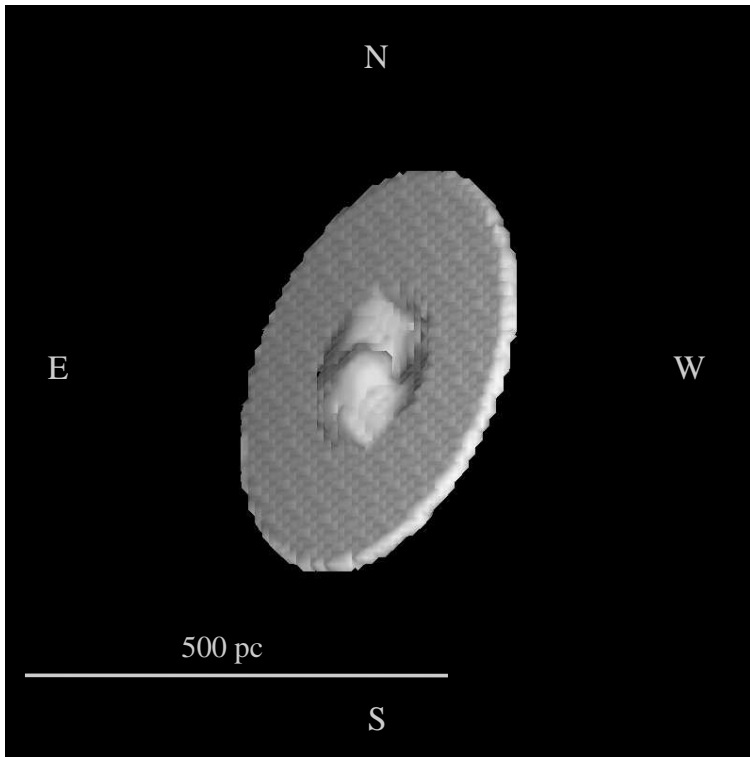


Fig. 18.— Spatial geometry of the warp model of NGC 3227. Bright colors of the warped disk indicate sections that are closer to the observer, darker colors those further away.

Table 1: Properties of NGC 3227

|                                | NGC 3227               |
|--------------------------------|------------------------|
| Right ascension (J2000)        | $10^h 23^m 30.6^s$     |
| Declination (J2000)            | $19^\circ 51' 53.99''$ |
| Classification                 | SAB(s) pec             |
| Inclination                    | $56^\circ$             |
| Position angle                 | $158^\circ$            |
| AGN type                       | Sey 1.2                |
| Systemic velocity $v_{sys;HI}$ | 1135 km/s              |
| Distance                       | 17.3 Mpc               |
| 1'' equals                     | 84 pc                  |

The sky coordinates, the systemic velocity as well as the Seyfert type were taken from NED (NASA/IPAC Extragalactic Database). The classification is from the RC3 catalog (de Vaucouleurs et al. 1991). Inclination and position angle are taken from Mundell et al. (1992b). For the distance we adopted the value of the LGG 193 group (Garcia 1993) were NGC 3227 is a member.

Table 2: Components of the  $^{12}\text{CO}$  line emission in NGC 3227

| Component              | R.A.<br>["] | DEC.<br>["] | $S_{\text{CO}}\Delta v$<br>[Jy km/s] | $\frac{\text{CO}(2-1)}{\text{CO}(1-0)}$ | $M_{H_2}$<br>[ $10^7 M_\odot$ ] | $M_{\text{dyn}}$<br>[ $10^8 M_\odot$ ] |
|------------------------|-------------|-------------|--------------------------------------|---|---------------------------------|--|
| nuclear region         | 0.0         | 0.0         | 3.8                                  | 0.7                                     | 0.19                            | 0.34                                   |
| ring                   | 0.0         | 0.0         | 55                                   | 0.4                                     | 8.49                            | 44.0                                   |
| red knot               | 0.0         | 1.0         | 4.9                                  | 0.5                                     | 0.37                            |  |
| molecular bar          | 6.0         | 0.1         | 6.2                                  | 0.6                                     | 0.95                            |  |
| NW-region              | -8.0        | +3.0        | 11                                   | 0.3                                     | 1.70                            |  |
| SE-region              | +12.0       | +10.0       | 6.8                                  | –                                       | 1.06                            |  |
| S-region               | 0.0         | -5.0        | 1.2                                  | 1.3                                     | 0.18                            |  |
| $8.4'' \times 8.4''$   | 0.0         | 0.0         | 75                                   | 0.5                                     | 11.60                           | 44.0                                   |
| $24.4'' \times 24.4''$ | 0.0         | 0.0         | 98                                   | –                                       | 15.20                           |  |

Listed are the centroid positions of individual source components, as separated by modeling (with 3DMod). The intensities of the  $^{12}\text{CO}$  lines given here are not corrected for the different beam sizes. However, this correction was taken into account for the line ratio. The intensity of the ring was measured in a disk with  $r=1.5''$  in the circular intensity map of gas that is in a disk with pure circular rotation (see Fig. 10). With the possible exception of the NW-, and SE-regions all other source components are not part of a simple circular rotating disk. The corresponding  $H_2$  masses of the individual components are derived in section 5. The estimated errors of the integrated line intensity values are 15% for the  $^{12}\text{CO}$  (1-0) line and 30% for the  $^{12}\text{CO}$  (2-1) line. For each component the flux and the obtained molecular  $H_2$  mass  $M_{H_2}$  is given. In addition we give the dynamical mass  $M_{\text{dyn}}$  if possible.

## APPENDIX

Here we give a detailed description of the algorithms we used to analyze (Appendix A) and describe (Appendix B) the kinematics and intensity distribution of the molecular gas in the nuclear region of NGC 3227. We also summarize and compare possible physical mechanisms that may lead to a warp of the molecular disk in the circum-nuclear region of active galactic nuclei (Appendix C).

### A. DECOMPOSITION OF MOTIONS: 3DMod

The application of 3DMod allows us to decompose the observed kinematics into their components of non-circular motion and circular rotation around the nuclear position. As an input it uses information on the integrated line flux distribution, the rotation curve and the spatial distribution of the velocity dispersion. The 3-dimensional spatial distributions of the intensity, the velocity and the velocity dispersion are generated separately.

**Intensity distribution:** We use the deprojected measured intensity distribution. We correct for resolution dependent deprojection effects by deconvolution before the deprojection and a later reconvolution. The de-projected deconvolved intensity map is loaded into the  $xyz$  model cube also allowing to introduce a thickness of the molecular disk in the  $z$  direction, if required.

**The velocity field:** The spatial velocity cube is constructed assuming that the gas is dynamically coupled via interaction between the individual molecular clouds and clumps and that the velocity field does not vary significantly with height  $z$ . The rotation curve is extrapolated to  $v = 0 \text{ km/s}$  towards the origin ( $r = 0$ ) and used to model the axisymmetric velocity field in the plane of the galaxy assuming circular rotation.

**Velocity Dispersion:** We assume that the velocity dispersion of the gas is locally isotropic. We allow for a possible exponential variation  $\sigma(x, y, z) = A \times r(x, y, z)^{-\alpha}$ . Here  $r(x, y, z)$  is the radial distance from the origin. Such a description is appropriate for the transition between a possibly large nuclear velocity dispersions and the low dispersions in the disk. A minimum velocity dispersion of  $7 \text{ km/s}$  is assumed for the dispersion between the individual clouds (e.g. Combes & Bica 1997).

**Creation of Model Cubes:** Each spatial cube is corrected for inclination  $i$  and position angle  $PA$  of the galaxy. After rotation the 3 individual spatial cubes are merged to obtain a  $xyv$  cube with two spatial axes (on the sky) and a spectral axis. The spectral with a resolution similar to the observed data is generated via integration along the line of sight. For each spatial pixel in the plane of the sky the central velocity is determined and the flux is distributed into the spectral pixels according the local velocity dispersion. Convolution along the remaining two axis gives the required spatial resolution. After scaling to the observed flux the calibrated model  $xyv$  cube can directly be compared to the measured data.

**Decomposition of Motions:** The  $xyv$  cube is generated as described above assuming that all the flux is originating from gas in circular motion. The difference between the data



cube and the model cube then shows positive and negative residuals at all positions for which the assumption of circular motion is not correct. In general it can be demanded that the integrated flux at each position is positive. This means that the positions which have negative residuals have to be corrected. As a first approximation of the correction we create an intensity map of the negative residuals by integrating them over velocity, subtracting a mean negative noise level, and then setting all positive values in the resulting map to zero. This map is added to the observed intensity map. The new map should now contain only emission from components in circular motion and is used as a new input to calculate the intensity cube. Then a new  $xyv$  cube is generated and subtracted from the data cube. The residual cube should now contain only significant positive residuals which represent components in non-circular motion.

## B. KINEMATIC MODELING: 3DRings

The model 3DRings allows to create kinematic models of circular and non-circular motions. The model is based on the following considerations: Since gas is dissipative it can only move for a longer time on orbits which are not self-intersecting, not crossing and do not have strong cusps. Therefore only two basic possibilities are available for gas orbits: (1) planar circular or elliptical orbits and (2) tilted circular orbits. The first possibility can be identified with the  $x_1$  and  $x_2$  orbits (e.g. Contopoulos & Papayannopoulos 1980) which exist in bar potentials in the plane of the host galaxy. The second possibility describes gas motion that is no longer confined to the plane of the galaxy so that the gas disk is warped. We use the inclination, position angle, and the rotation curve derived from the molecular gas velocity field. The gas disk is subdivided into a number of elliptical (bar approach) or circular (warp approach) rings between a given inner and outer radius. For both approaches the properties of these 3-dimensional rings are given by continuous parameter input curves as a function of radius. The fitting is started at large radii where simple circular motion dominates and successively extended towards the nuclear region. The fit is done matching the pv-diagrams and the moment maps.

**The bar approach:** Rather than calculating the gas motion in a given gravitational, potential 3DRings fits the observed  $xyv$  data cube under the simplifying assumption of closed elliptical  $x_1$  and  $x_2$  orbits with continuous curves of ellipticity  $\epsilon(r)$  and position angle  $PA(r)$  and centered on the nucleus. This approach has been adopted from Telesco & Decher (1988; Fig. 7 therein) who discussed its validity in great detail. To match observations and theoretical calculations we implemented the orbits such that the velocities at the minor and major axis are inversely proportional to the axial ratio.

**The warp approach:** 3DRings is similar to other tilted ring models (e.g. Rogstad et al. 1974 Nicholson, Bland-Hawthorn, Taylor 1992, see also Fig. 16 in Schwarz 1985) and follows the method described in Quillen et al. (1992). The inclination and precession of the rings (representing gas orbits) is given by continuous curves  $\omega(r)$  and  $\alpha(r)$ , respectively (see Fig. 19). A torque acting on an orbit with a circular velocity  $v_c(r)$  introduces a precession rate  $d\alpha/dt \sim \xi v_c/r$ . After a time  $\Delta t$  one obtains  $\alpha(r) = \xi \Omega \Delta t + \alpha_0$ . Here  $\xi$  is given by the acting torque (see Appendix C) and  $\Omega = v_c/r$ . We considered for our analysis models with constant traveling time  $\xi \Delta t$  and assume the molecular gas to be uniformly distributed.

**Verification of the bar approach:** To test how far our simplified bar models that follow the original approach of Telesco & Decher (1988) are justified, we compare them to theoretical calculations. In our model continuous, smoothly varying curves of the ellipticities and position angles of the 3DRings ellipses were chosen under the boundary condition that they do not cross each other. The resulting model resembles the intensity map and velocity field of theoretical models (e.g. *Model 001* of Athanassoula 1992b). The velocity field is shown in the rest-frame of the rotating bar by subtracting a circular disk model with constant intensity and a linearly increasing rotation curve which results in the same angular velocity as the bar model at the co-rotation radius of the bar model (Fig. 20). We also compare the density and velocity profile across the dust lane. Due to shocks jumps in the density and velocity profile occur at the position of the dust lanes (Fig. 21). The density

profile shows a maximum at that position whereas the velocity has its maximum upstream and adopts much smaller values downstream with respect to the shock in the dust lane. As shown in Fig. 20 and 21 the results of 3DRings are also qualitatively comparable to the ones of Athanassoula (1992b). Therefore we are confident that our chosen bar approach is in sufficient agreement with results of theoretical calculations and N-body simulations and *very well suited to search for bar signatures in the observed  $xyv$  cubes without having to calculate orbits in assumed or inferred gravitational potentials.*

### C. CAUSES FOR WARPS IN CIRCUM-NUCLEAR GAS DISKS

Since a warped molecular gas disk in the circum-nuclear regions of galaxies is a relatively new concept we give a more detailed description of possible causes for warps in the area between a few to several 100 pc. To generate a warp in a thin gas disk it has to be moved out of the plane of the galaxy by an acting torque. Several mechanisms can account for a torque in the central few hundred parsecs. The most important ones are the gas pressure of the ionization cone, radiation pressure of a radio jet or a nuclear source, the gravitational forces of individual molecular cloud complexes and an axisymmetric, non-spherical galactic potential (e.g. representing the stellar bulge of a galaxy). In general the torque  $M$  can be expressed as

$$|\vec{M}| = |\vec{F} \times \vec{l}| = |\vec{F}| \cdot l \cdot \sin(\psi) \approx p \cdot A \cdot l \quad (\text{C1})$$

For this approximation we assume that the force  $\vec{F}$  is perpendicular to the lever arm  $\vec{l}$  (i.e.  $\psi = 90^\circ$ ). In addition the force can be expressed by a pressure  $p$  onto the local disk area  $A$  relating the torque to a pressure gradient between the top and bottom side of the disk. For the different mechanisms, we describe in the following approximations of the torques as well as the related observational quantities that are required for this. The results of the calculations are summarized in Tab. 3 and Tab. 4. Only the torque by the gas pressure can sustain a warping of the disk over several dynamical time scales. As a transient phenomenon a GMC above or below the disk may induce a torque as well.

#### C.1. Warp caused by an axisymmetric galactic potential

The observed HI-Warps are explained by this mechanism (see review by Binney 1992). The axisymmetric potential (Fig. 22 a) of the halo applies a torque to the HI gas disk evoking a warping of the HI disk. The derivation of the torque is given in Goldstein (1980) and in Arnaboldi & Sparke (1994). The torque  $M$  induced by a mass  $m$  at a point  $(r, \theta)$  with the inclination  $\theta$  of the rotation axis of the orbit of the mass  $m$  relative to the rotation axis of the main system is here defined as  $M \sim m \frac{\delta V}{\delta \theta}$  (Stacey 1969). Here  $V$  is the axisymmetric potential. Arnaboldi & Sparke (1994) deduced in their analysis of orbits in polar rings in an axisymmetric potential the torque far outside of the core of a slightly oblate halo. For a potential with oblate symmetry (axial ratio  $a = b \neq c$ ) the torque is described by

$$M \sim m\pi G\rho_o \frac{a^2(a^2 - c^2)}{3c^2} \sin(2\theta). \quad (\text{C2})$$

This relation is adequate to estimate the strength of an axisymmetric potential outside the core radius. Inside the core radius of the potential (halo) the torque varies with  $\sim r^2$  (Sparke 1996). The author also gives a relation between the precession rate and the torque:

$$M \sim m\dot{\Phi}\sin(\theta)(r^2\Omega(r)). \quad (\text{C3})$$

Here  $\dot{\Phi}$  is the precession rate (in units of [rad/s]) and  $\Omega(r) = \frac{v(r)}{r}$  is the angular velocity. Since these quantities are known or used as input parameters for 3DRings (see Appendix B), the above relation can be used to estimate the torque of the observed or modeled (with 3DRings) warp. We neglected the effects of dissipation, radial mass transport (only circular orbits are used) and self-gravity within the rings. Both relations can only give rough estimates as the core size of the axisymmetric potential is unknown or the precession rate  $\dot{\Phi}$  (some fraction of  $\frac{2\pi}{T}$ ;  $T$  is the time of circulation of a circular orbit) and the inclination angle  $\theta$  have to be determined from the model 3DRings. However, for a first approximation these estimates can be used as reference values in order to determine whether a given mechanism is sufficient to account for the required torques.

### C.2. Torque imposed by a molecular cloud

As a transient phenomenon a GMC above or below the disk may induce a torque as well (Fig. 22 b). The decomposition of the motions in the molecular gas in NGC 3227 (see section 5 and Appendix A) has shown that in the inner 300 pc molecular cloud complexes exist that do not participate in the circular motion of the underlying molecular gas disk. Therefore these complexes are likely not to be part of the gas disk but they are probably located above or below the disk. In this case they interact gravitationally with the underlying gas disk and can result in a warp. Under the assumptions that the mass  $m_{GMC}$  of the GMC is similar to the mass  $m$  of the underlying gas disk segment and that the GMC has a height above the disk of the order of its radius the acting force between the GMC and the disk section can simply be estimated via

$$F = G \frac{m_{GMC} \cdot m}{r^2} . \quad (\text{C4})$$

This then allows us to estimate the torque following equation C1. The mass of the GMC can be estimated from the  $^{12}\text{CO}$  line flux (see section 6).

### C.3. Warp caused by gas pressure

In active galaxies ionization cones ranging from the nucleus till a distance of a few hundred parsecs are observed. These cones can be regarded as parts of the NLR (narrow line region) for which the number density  $n$  and excitation temperature  $T$  can be deduced from the observed forbidden lines. The cones have partly large opening angles and show in general a large inclination relative to the normal axis on the disk. In many cases the cones can touch or even intersect the disk. Then there will be a pressure gradient between

the top and bottom part of the disk (Fig. 22 c). Even if the molecular gas is clumpy the response of clumps to the pressure gradient imposed by the gas in the ionization cone can be substantial (e.g. Eckart, Ageorges, Wild 1999) and due to self-gravitative interaction (e.g. Lovelace 1998) the entire molecular disk will response. In this case the gas pressure applies a force at a distance  $r$  from the center onto the disk. Via a torque  $\vec{M}$  this causes a change of the angular momentum  $\vec{L}$ . This process can be stable over time-scales which are long compared to the dynamical time-scales at the corresponding radii. Therefore this scenario is very well suited to cause and maintain warps in circum-nuclear molecular gas disks. Such a scenario has also been proposed by Quillen & Bower (1999) for M 84. To first order the gas pressure can be estimated from the equation of state for an ideal gas

$$p = \frac{N}{V} \cdot k \cdot T = n \cdot k \cdot T \quad (\text{C5})$$

The number density  $n$  can be derived from the particle number  $N$  per volume  $V$  and  $k$  is the Boltzmann constant. The torque can then again be calculated following equation C1. The area  $A$  is the interaction area of the ionization cone with the galaxy disk and  $l$ , the lever arm, is the distance to the center of this area. For a purely geometrical dilution of the number density it can be shown that the torque is independent of the radial distance from the center. The ionization cone and its influence on the disk can therefore extend over a few 100 pc and thus provide a continuous warping of the gas disk.

#### C.4. Warp caused by radiation pressure

In the case of a 1 pc diameter circum-nuclear accretion disk a warping of the disk can be caused by non-uniform illumination of the gas disk by the AGN radiation field (UV, X-ray; Pringle 1996, 1997; Fig. 22 d). This is due to the fact that independent of the angle of incident photons are irradiated perpendicular to the disk (Pringle 1996). The non-uniform illumination can be evoked via a non-isotropic radiation field of the AGN or via a small instability in the disk that moves gas out of the plane (as shown here). Due to extinction in the disk this process can not act at large distances from the nucleus. The radio jet, however, may represent a possibly strong radiation source. If the jet is inclined with respect to the gas disk the jet components can be quite close to the disk even at large radii from the nucleus (Fig. 22 d). Therefore we estimate the jet's possible contribution to the warping of the gas disk. To calculate the radiation pressure of the jet its radiation power has to be estimated first. We assume that the radiation flux density  $S$  is given by a power law  $S = b \cdot \nu^\alpha$ . We assume synchrotron emission and  $\alpha \sim -1$ . In order to obtain an upper limit to the torque induced by a jet we also assume that the upper cut-off frequency is in the NIR to optical range as it is found for powerful jets (e.g. M87; Meisenheimer et al. 1996). In the radio to sub-mm range the disk can be regarded as being transparent. To estimate the total luminosity we used integration limits of  $10 \mu\text{m} - 0.5 \text{ mm}$ . For isotropic radiation the jet luminosity is given via  $L = 4\pi D^2 \int_{\nu_1}^{\nu_2} S d\nu = 4\pi D^2 \int_{\nu_1}^{\nu_2} b \cdot \nu^\alpha d\nu$  Here  $D$  is

the distance to the source. The radiation density  $I$  onto a given area  $A$  (seen under a given solid angle from the jet) at distance  $l$  can now be calculated. The radiation pressure is then estimated via:

$$p = \gamma \frac{I}{c}. \tag{C6}$$

Here  $\gamma$  equals 1 in the cause of a black body, 2 for an ideal reflecting body and  $c$  is the speed of light. Again equation C1 can be used to obtain an upper limit of the torque due to radiation pressure from the jet.

E1

---

<sup>E1</sup>NOTE TO EDITOR: The following captions and figures belong to the appendices.



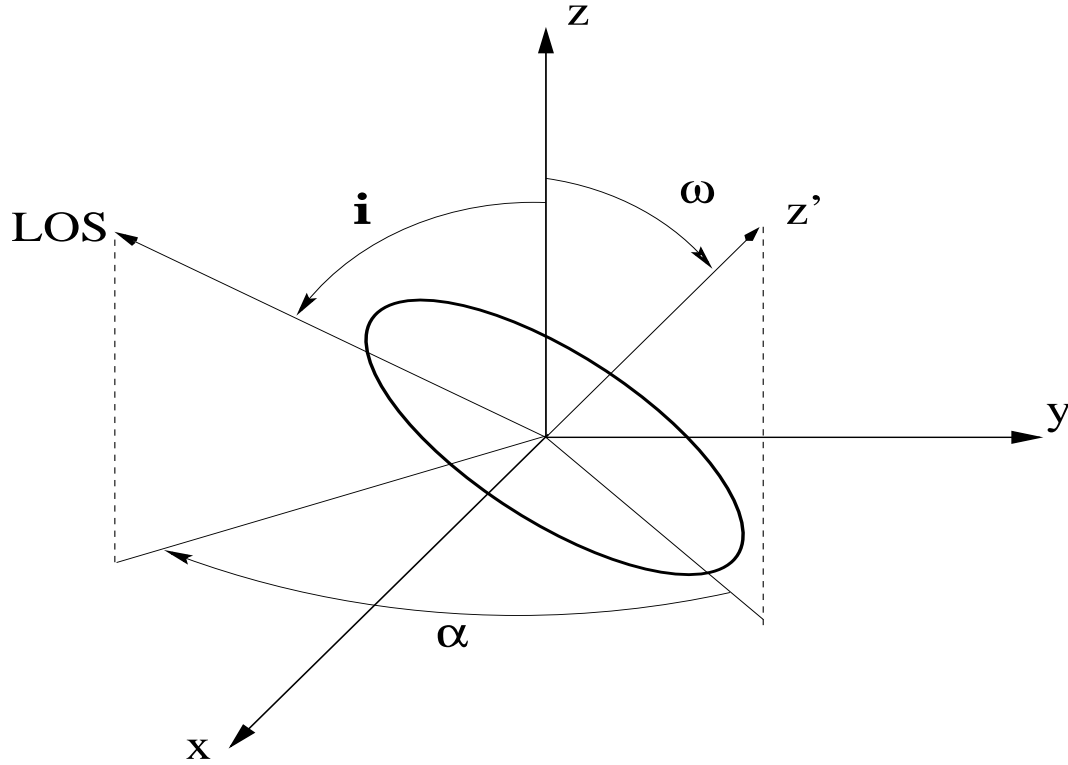


Fig. 19.— Important quantities for the warp approach of the model 3DRings. A single ring is shown which is tilted by an angle  $\omega$  relative to the rotation axis of the galaxy which is inclined to the line of sight by the angle  $i$ . Here  $\alpha$  is the precession angle between the ring axis and the projection of the line of sight onto the plane of the galaxy.

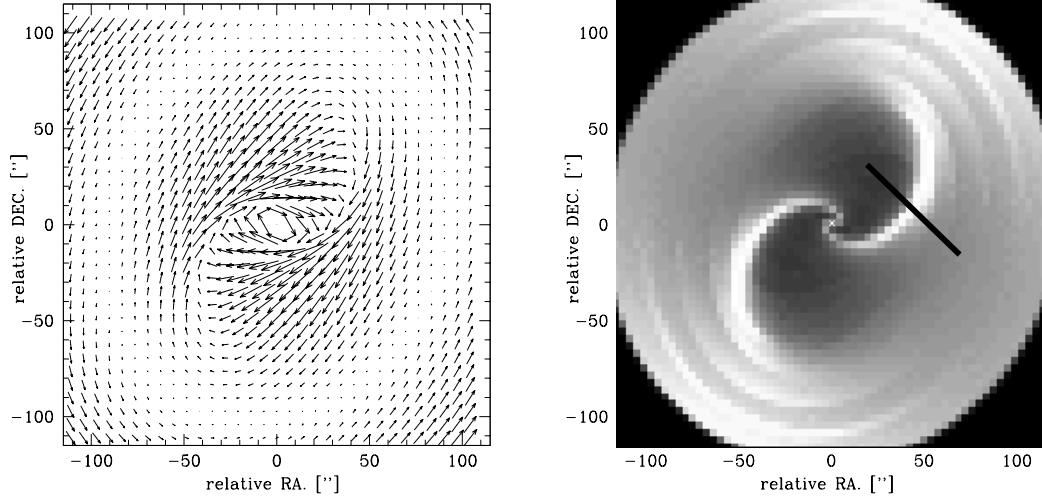


Fig. 20.— Density distribution (right) and the velocity field (left) obtained from our model bar approach (from 3DRings). These results are comparable to *Model 001* from Athanassoula (1992b). As in Athanassoula (1992b) we subtracted from the total velocity field the field of a rigid rotating disk with the angular velocity  $\Omega_P$  at the CO-rotation. In the density distributions (right) the slit positions for Fig. 21 are indicated by a thick line.

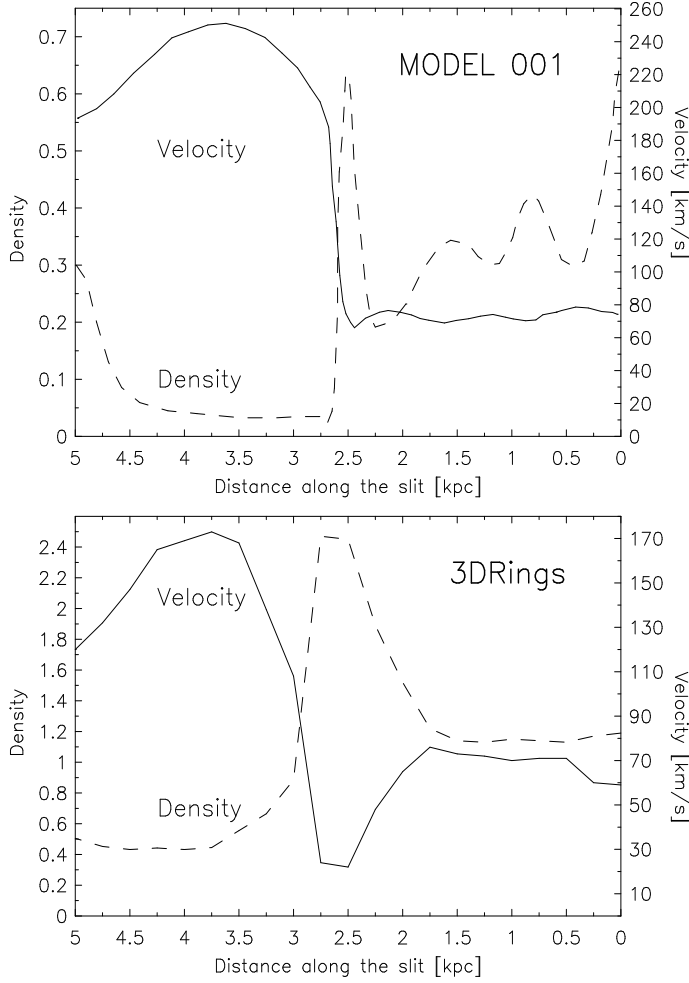


Fig. 21.— Comparison of the shock fronts between the *Model 001* from Athanassoula (1992b) and our model calculations. Along the slit across the shock front (indicated in Fig. 20) the velocities (solid line) as well as density distributions (broken line) in *Model 001* (top) are shown for from SW (left) to NE (right). In both cases the abrupt increase of the density as well as the strong drop in the velocity is seen at the position of the shock front. This demonstrates that the bar approach of 3DRings provides qualitatively (and within tolerable limits also quantitatively) similar results as more complex theoretical calculations. Thus 3DRings can be used to search for bars via the fitting of the 3 dimensional data cube ( $xyv$  cube).

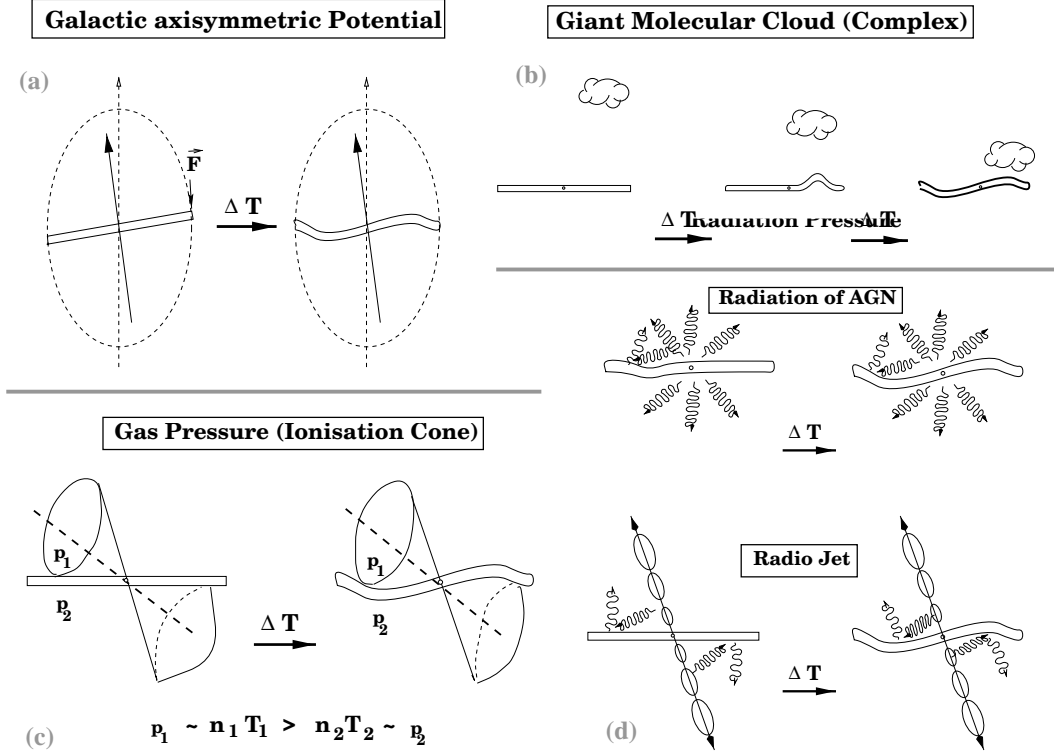


Fig. 22.— (a) Influence of an axisymmetric potential onto a rotating gas disk. If the rotating axis of the gas disk is misaligned to the figure axis of the potential, this leads to a warping of the gas disk after a time  $\Delta T$ .

(b) Influence of a molecular cloud onto a rotating gas disk. A molecular cloud which is located above the gas disk applies a force onto the disk. Within a dynamical time-scale a warp in the disk develops. Here we assume that the height of the cloud is of the order of its radial distance to the nucleus. This time-scale over which the warp develops is about equivalent to the orbital time scale of the gas in the disk at the given radius as well as the time-scale in which the cloud is settling into the gas disk. Dissipative interaction of the cloud with the disk lead to the fact that this is only a transient phenomenon.

(c) Influence of an ionization cone onto a rotating gas disk. In this scenario the ionization cone is in touch with the gas disk. Due to the higher product of particle densities  $n_1$  and temperatures  $T_1$  in the cone a pressure gradient exists between the top and bottom part of the disk. Because of the pressure difference ( $p_1 - p_2$ ) acting on the interaction area a force and therefore a torque develops leading after a time  $\Delta T$  to a warping of the gas disk.

(d) Influence of the radiation pressure onto a rotating gas disk.

*Top:* In the case of a circum-nuclear accretion disk a warping of the disk can be caused by non-uniform illumination of the gas disk by the AGN radiation field (UV, X-ray; Pringle 1997).

*Bottom:* At larger distances the radio jet which lies out of the plane of the gas disk can be regarded as a possible radiation source. In this case non-uniform illumination of the gas disk is given such that a warping mechanism - similar to the one described above - acts.

E2

Table 3: Causes for the warp in NGC 3227

| Cause                        | Property                  |                    | Value                                     |
|------------------------------|---------------------------|--------------------|---|
| Estimated via                |                           |                    |   |
| <b>3DRings<sup>a</sup></b>   | <b>torque<sup>1</sup></b> | $M$                | <b><math>6.4 \times 10^{46}</math> Nm</b> |
|                              | molecular gas mass        | $m$                | $2.0 \times 10^6$ M <sub>⊙</sub>          |
|                              | radius                    | $r$                | $7.7 \times 10^{17}$ m                    |
|                              | velocity                  | $v(r)$             | 60 km s <sup>-1</sup>                     |
|                              | orbital time scale        | $\dot{\Phi}^{-1}$  | $1.8 \times 10^{13}$ s                    |
| <b>Potential<sup>b</sup></b> | <b>torque<sup>2</sup></b> | $M$                | <b><math>3.0 \times 10^{10}</math> Nm</b> |
|                              | molecular gas mass        | $m$                | $2.0 \times 10^6$ M <sub>⊙</sub>          |
|                              | volume                    | $V_o$              | $2.9 \times 10^{36}$ m <sup>3</sup>       |
|                              | total mass                | $m_o = \rho_o V_o$ | $3.4 \times 10^7$ M <sub>⊙</sub>          |
| <b>GMC<sup>c</sup></b>       | <b>torque<sup>3</sup></b> | $M$                | <b><math>1.4 \times 10^{46}</math> Nm</b> |
|                              | cloud mass                | $m_{GMC}$          | $3.7 \times 10^6$ M <sub>⊙</sub>          |
|                              | force                     | $F$                | $5.4 \times 10^{26}$ N                    |
|                              | lever arm                 | $l = r$            | $2.6 \times 10^{18}$ m                    |

See caption in Tab. 4

---

<sup>E2</sup>NOTE TO EDITOR: The following two tables should be one (Tab.8); table caption is incomplete in the processed file (ps-file)

Table 4: Causes for the warp in NGC 3227

|                                       |                           |               |   |
|---------------------------------------|---------------------------|---------------|---|
| <b>Gas pressure<sup>d</sup></b>       | <b>torque<sup>4</sup></b> | $M$           | <b><math>1.2 \times 10^{46}</math> Nm</b> |
|                                       | particle density          | $\frac{N}{V}$ | 1000 cm <sup>-3</sup>                     |
|                                       | temperature               | $T$           | $1.4 \times 10^5$ K                       |
|                                       | gas pressure              | $p$           | $1.9 \times 10^{-9}$ Nm <sup>-2</sup>     |
|                                       | area                      | $A$           | $4.7 \times 10^{36}$ m <sup>2</sup>       |
|                                       | lever arm                 | $l$           | $1.3 \times 10^{18}$ m                    |
| <b>Radiation pressure<sup>e</sup></b> | <b>torque<sup>5</sup></b> | $M$           | <b><math>1.2 \times 10^{39}</math> Nm</b> |
|                                       | spectral index            | $\alpha$      | $\sim -0.9$                               |
|                                       | constant                  | $b$           | $8.4 \times 10^{-19}$ Wm <sup>-2</sup>    |
|                                       | luminosity                | $L$           | $8.4 \times 10^{30}$ W                    |
|                                       | intensity                 | $I$           | $4.0 \times 10^{-7}$ Wm <sup>-2</sup>     |
|                                       | radiation pressure        | $p$           | $1.3 \times 10^{-15}$ Nm <sup>-2</sup>    |
|                                       | area                      | $A$           | $6.7 \times 10^{35}$ m <sup>2</sup>       |
|                                       | lever arm                 | $l$           | $1.3 \times 10^{18}$ m                    |

<sup>a</sup> eq. C3; <sup>b</sup> eq. C2; <sup>c</sup> eq. C1 and C4; <sup>d</sup> eq. C1 and C5; <sup>e</sup> eq. C1 and C6

<sup>1</sup> from the parameters of 3DRings for a nuclear disk and a radius of 25 pc.

<sup>2</sup> from the nuclear molecular gas mass and the dynamical mass in a radius of 25 pc. (See section 6.) We used  $M \sim m\pi G\rho_o$  to get the order of magnitude.

<sup>3</sup> from the molecular gas mass of the redshifted knot and its distance (84 pc) from the nuclear gas disk (see section 6).

<sup>4</sup> particle density and temperature of the ionization cone from Gonzalés-Delgado & Pérez (1997), area ( $\sim (0.7'' \times 1.0'')$ ) and distance ( $\sim 0.5''$ ) from HST [O III] map (Schmitt & Kinney 1996).

<sup>5</sup> spectral index (for calculation we assumed  $\alpha = -1.0$ ) and constant  $b$  as well as area (about  $0.5'' \times 0.2''$ ) to match the radio jet (Mundell et al. 1992b) at a distance of 42 pc.